Title
Structural characterization of membrane proteins and antibody-antigen complexes using single particle electron microscopy

Author
Green, Evan Michael

Publication Date
2019

Peer reviewed|Thesis/dissertation

Structural characterization of membrane proteins and antibody-antigen complexes using single particle electron microscopy

by
Evan Michael Green

DISSERTATION
Submitted in partial satisfaction of the requirements for degree of
DOCTOR OF PHILOSOPHY

in

Biophysics

in the

GRADUATE DIVISION
of the
UNIVERSITY OF CALIFORNIA, SAN FRANCISCO

Approved:

DocuSigned by:
Yifan Cheng
37327FF78C17460...

Yifan Cheng
Chair

DocuSigned by:
Charles Craik
DocuSigned by:
Adam Frost
1E2FF75D7B5A48F...

Charles Craik

Adam Frost

Committee Members

Acknowledgements

First of all, I want to thank my thesis advisor Yifan Cheng. Yifan has given me tremendous freedom to pursue the topics I found most interesting during the course of my Ph.D. Outside of his scientific mentorship Yifan has been a fantastic role model as an upstanding person and member of the scientific community. His enthusiasm and scientific curiosity has been contagious and will stay with me well after I leave UCSF.

I also want to thank my previous scientific mentors including Martina Ralle, Arthur Glasfeld, and Eric Gouaux for giving me the opportunity to learn how to do scientific research in a variety of contexts. All of these individuals have greatly impacted my career and without their support I would have never been able to pursue a Ph.D. I have had the great fortune to have many scientific mentors and collaborators during my time at UCSF including Robert Stroud, Adam Frost, James Fraser, and Deanna Kroetz. I particularly want to thank Charly Craik for providing incredible support and encouragement from my qualifying exam until to my dissertation.

The Cheng lab has been a wonderful place to work for the past five years. I have learned invaluable skills from my lab mates over the years. While everyone in the lab has been critical to my development as a scientist, I want to particularly thank a number of post docs in the lab including Henriette Autzen, Amber Smith, Melody Campbell, Jean-Paul Armache, Zanlin Yu and David Bulkley for countless hours of discussions, suggestions, and support. My fellow graduate students Eugene Palovcak, Daniel Asarnow, Yuan Gao and Bryan Faust have always reminded me that scientific research should be a fun endeavor filled with crazy ideas and lasting friendships.

Both inside and outside of the lab I have amassed a number of great friends and collaborators over the course of my Ph.D. There are too many people to name but I want to specifically thank my many collaborators including Alex Kintzer, Pawel Dominik, Koli Basu, Meghna Gupta, Dong Hee Chung, Nancy Li, Natalia Sevillano and Ruchika Bajaj along with my friends Ben Barad, Ilan Chemmmama, Sasha Dickinson, Sergei Pourmal, Paul Thomas, Erin Thompson, Lakshmi Miller and Amelia Munson. Some of my fondest memories while at UCSF were from the time living with my fellow classmates Lillian Kenner, Stefan Niekamp and Eugene Palovcak on top of Potrero Hill.

Of course, none of this would have been possible without the support and encouragement of my family. My parents, Sharon and Tim, and my brothers, Sean and Ian.

Contributions

Chapter 1

Koli, B.; Green, E.M.; Cheng, Y.; Craik, C.S.; 2019. Why recombinant antibodies — benefits and applications. *Curr. Opin. Biotechnol*. 60:53-158.

Chapter 2

Kintzer, A.F.; Green E.M.; Dominik, P.K.; Bridges, M.; Armache, J.P.; Deneka, D.; Kim, S.S.; Hubbell, W.; Kossiakoff, A.A.; Cheng, Y.; Stroud, R.M. 2018. The structural basis for activation of voltage sensor domains in an ion channel TPC1. *PNAS*. 115(39):E9095-E9104.

Structural characterization of membrane proteins and antibody-antigen complexes using single particle electron microscopy

Evan Michael Green

Abstract

Proteins are the macromolecular complexes responsible for carrying out the majority of cellular processes ranging from signal transduction to catalyzing metabolic reactions and DNA replication. Proteins are polymers made up of amino acids that adopt complex three-dimensional shapes which are critical for their function. To better understand the structure and function of proteins structural biologist use a wide variety of experimental tools including NMR spectroscopy, X-ray crystallography, and electron microscopy (EM). Until recently, the majority of our understanding of protein structure was derived from X-ray crystallography but recent technological advances in electron microscopy have made it possible to determine the structure of a wide range of proteins to near-atomic resolution. During my Ph.D. I have primarily been focused on studying the structure and function of membrane proteins and antibody-antigen complexes using both negative stain EM and cryogenic EM (cryoEM).

The first chapter of this dissertation focuses on the utility of recombinant antibodies and their ability to probe protein structure and function in a wide variety of contexts. In particular, recombinantly expressed antibodies have a number of distinct advantages over those derived from the hybridoma approach. Of particular relevance to my thesis work I highlight the use of recombinant antibodies to study the structure of protein complexes with for single particle cryoEM.

In the second chapter I describe the structural characterization of the two-pore channel TPC1 from *Arabidopsis thaliana* (AtTPC1). AtTPC1 is a voltage- and ligand-gated ion channel.

Previous structures of this channel revealed the first resting state of a voltage sensor in an intact ion channel. The work in this chapter expands on the previous research by mutating the luminal Ca^{2+} binding site shifting the open probably of the channel at 0 mV in order to chapter an activated voltage senor. Using single particle cryoEM, and a high-affinity recombinantly expressed antibody fragment, we determined two new structures of the voltage sensor. This information provided critical information about the voltage activation mechanism for ion channels and represented one of the first examples of a single voltage gated ion channel trapped in multiple conformations.

In the third chapter I present some unpublished work on a new immunoprecipitation-based method to rapidly characterize recombinant antibodies identified from phage display libraries. This method takes advantage of the minimal sample requirements of negative stain EM in order to give information about the epitope that the Fab binds as well as an estimate for the relative affinity. The technique greatly increases the rate at which it is possible to go from a panning to selecting the most useful Fabs to be used for structure determination using single particle cryoEM.

Table of contents

List of figures

List of tables

Chapter 1

Why recombinant antibodies — benefits and applications

Contributing Authors

Koli Basu[1,*], Evan M. Green[1,*], Yifan Cheng[2,3], and Charles S. Craik[1]

[1]Department of Pharmaceutical Chemistry, University of California, San Francisco

[2]Department of Biochemistry and Biophysics, University of California, San Francisco

[3]Howard Hughes Medical Institute, University of California, San Francisco

[*] Equal contribution

Abstract

Antibodies (Abs) are ubiquitous reagents for biological and biochemical research and are rapidly expanding into new therapeutic areas. They are one of the most important probes for determining how proteins function under normal and pathophysiological conditions. Abs are required for quantification of targets, detection of temporal and spatial patterns of protein expression in cells and tissues, and identification of interacting partners and their biological activities. Their remarkable specificity and unique binding properties can facilitate three-dimensional structure determination using X-ray crystallography and electron cryomicroscopy. While hybridoma technology that involves animal immunization is often productive, many antigen targets do not generate useful Abs. This is particularly true if unique states of the target or critical non-immunogenic target sequences need to be recognized by the Abs. By using the methods of recombinant antibody generation, identification, and engineering, these 'hybridoma-refractory' antigens can be readily targeted. Specific, reproducible, and renewable recombinant Abs are proving to be invaluable reagents in applications ranging from biological discovery to structure determination of challenging macromolecules.

Discussion

Comparing hybridoma and recombinant antibodies

Monoclonal, target-specific antibodies (Abs) are routinely developed through hybridoma technology[1] or by biopanning with recombinant antibody libraries [2,3]. For hybridoma antibody development, B-cells from animals are harvested several weeks after they have been inoculated with the antigen. Immortalized hybridoma cells are generated through the fusion of B-cells with a myeloma cell line. Each hybridoma cell normally secretes a single species of immunoglobulin G (IgG) and the secreted IgGs are used in binding assays, such as ELISA or FACS, to select for cell lines producing antigen binders[4,5]. Since the antibody generation and affinity maturation occurs *in vivo* through the animals immune response, these Abs can have high specificity and affinity[6].

A common theme in any antibody campaign is that the investigator will 'get what they screen for'. A significant drawback of hybridoma antibody campaigns is that the antigen will undergo proteolytic degradation to initiate the antibody-generating immune response (Fig 1) and the derived Abs may not recognize the native form of the antigen. Another disadvantage is that the Fragment of antigen-binding domain (Fab) (Fig 2) obtained by IgG proteolysis[7] may not retain the same antigen-binding properties as the IgG. A polypeptide sequence that does not generate an immune response or three-dimensional epitopes can make antigens particularly hybridoma-refractory. Furthermore, the utility and reliability of numerous commercial Abs, many of which are generated through hybridoma technology, can be limited since the specificity and cross reactivity of Abs vary from vendor-to-vendor and lot-to-lot[8].

Many of the pitfalls of hybridoma antibody generation are resolved through biopanning with recombinant antibody libraries[9,10]. These libraries are generated by cloning synthetic or naive

Fabs, single-chain variable fragments (scFvs), or nanobodies (Nbs) (Fig 2) into phage or yeast display vectors[11–14]. Antigen-binding Abs are enriched through several rounds of selection by solid-phase[2] or by flow cytometry[15,16] (Fig 1). Biopanning parameters can be selected for the desired antibody-antigen binding conditions. The ability to counter select against non-desired epitopes is a particularly powerful advantage of the biopanning approach. Counter selection can be accomplished using different conformation states, homologues, or specific domains[14,17]. Since the entire process is done *in vitro*, temperature, buffer conditions, antigen ligand concentrations, and oligomeric assembly can be readily controlled. With proper selection conditions, the antigen has a much lower chance of being altered through the recombinant biopanning process compared to the hybridoma approach of animal inoculation. Recently, advances in automating the recombinant antibody biopanning process has greatly reduced the effort, time, and cost required[18].

Another advantage of using a recombinant antibody library is that binders from the biopanning process can be easily characterized through DNA sequencing. Once the sequence of the antibody is known it is essentially immortalized, renewable, and can be produced in recombinant expression systems. Recombinant expression of Fabs, scFVs, and Nbs in *Escherichia coli* is a fraction of the cost of hybridoma Abs generation[19]. Recombinant Abs can be engineered to have additional functionalities including tags for purification or immunoprecipitation, conjugation sites to increase chemical space, or mutagenesis to map the determinants of antigen recognition. The antibody sequence allows for *in vitro* affinity maturation, mimicking an immune response, to select Abs with higher affinity and lower off-rate[20]. Abs derived from recombinant affinity maturation campaigns often have affinities 10-50 times higher than their parent[21]. Engineering of therapeutic antibody candidates can improve

their pharmaceutical effects, such as prolongation of half-life to increase their efficacy[22]. Further efforts to develop therapeutic Abs that take advantage of recombinant technologies have recently been reviewed[23].

Functional applications of recombinant antibodies

Since the advent of biopanning by phage and yeast display, recombinant Abs have become invaluable reagents for therapeutics, imaging, and understanding protein-protein mediated mechanisms of action (Fig 2). Therapeutic Abs typically prevent binding of ligands to receptors by either blocking the ligand or the receptor[24]. Abs against the immune checkpoint protein programmed death (PD-1) and its ligand (PD-L1) are recent examples[25]. Currently, there are several antibody therapeutics against these two targets for various cancer treatments that are either approved or in clinical trials[26], indicating the importance of this growing field. And with this, the development of tools for preclinical assessment of patient responses to immunotherapy is also emerging, such as immunopositron emission tomography (immunoPET)[27] where Abs towards the immune checkpoint proteins are conjugated with a radiotracer and used for *in vivo* imaging.

Recombinant Abs that recognize specific states of a protein can potentially be used as diagnostic tools. An example of this is a recombinant active-site-specific Fab developed for the transmembrane serine protease, matriptase[17]. Active matriptase is a biomarker for tumorigenesis. The recombinant Fab distinguished cancer from non-cancer cell lines *in vitro* and in colon cancer sections from human tissue micro arrays. *In vivo* imaging of colon cancer patient-derived xenograft models showed tumor uptake of the radio-labelled antibody, indicating that this Fab could be used for noninvasive tumorigenesis evalution[28].

Abs are also used for exploring the roles of specific intercellular and extracellular proteins. Blocking protein-protein interactions by Abs can help dissect the mechanism of action of the target of interest. By converting Abs to scFvs, intracellular signaling pathways can be probed since scFvs are properly folded in the reducing cytoplasmic environment, whereas IgGs and Fabs are not. An example of this is the intracellular expression of an scFv which was generated against β-arrestins (βarrs), an important regulator of GPCR (G protein-coupled receptor) signal transduction[29]. This scFv selectively disrupts βarrs/clatherin interaction and inhibits agonist-induced endocytosis of GPCRs without affecting other molecular pathways. Another such example of Fab-based modulation is of the Vif protein complex, which is an HIV protein complex that counteracts the antiviral effects of the host apolipoprotein B mRNA editing enzyme, catalytic polypeptide 3 (APOBEC3) immune proteins[30]. *In vitro* experiments with the Fabs, and *in vivo* experiments with transiently expressed scFvs, showed that Vif uses a multi-pronged approach involving both degradation-dependent and -independent mechanisms to suppress APOBEC3-innate immunity.

Cell classification and profiling, using a technique referred to as phage-antibody next generation sequencing (PhaNGS)[31], demonstrated yet another innovative use of recombinant Abs. In this technique, a collection of defined Fabs that bind specifically to previously identified targets of interest are displayed on phage and pooled to make a customized library. Fab-phage bound to cells are identified through next-generation sequencing of a barcode region in the Fab. It is expected that PhaNGS will be useful for observing surface protein changes in disease-state cells and for identification of new combinatorial biomarkers and drug targets.

Recombinant antibodies in X-ray crystallography

Abs are used extensively in structural biology to help determine high-resolution structures of antibody-antigen complexes owing to their ability to facilitate crystal packing of challenging targets, act as a fiducial marker to aid in particle orientation in electron microscopy (EM), and trap specific conformational states (Fig. 2). In the following sections, we highlight the broad utility of Abs for structural studies with a particular emphasis on recombinant Abs.

In order to determine the three-dimensional structure of a protein using X-ray crystallography, it is necessary to generate well-ordered crystals that diffract to high resolution. For this to occur, crystal contacts must be made between individual macromolecules to generate a three-dimensional lattice. Formation of crystal contacts can be impeded by a lack of suitable exposed surface area or by conformational flexibility. This is particularly true of detergent-solubilized membrane proteins as the detergent micelle often precludes crystal contacts between transmembrane helices[32]. Abs have been used to assist in the crystallization of membrane proteins since it was observed that the lattice contacts of membrane-protein crystal structures are often mediated by polar surfaces[33]. In the case of the potassium channel KcsA co-crystallization with a Fab was necessary to achieve the resolution required to assign potassium ion coordination in the central pore[34].

While early antibody-assisted crystallization studies used hybridoma derived Abs, there are a number of significant advantages for recombinant Abs. Since full length IgGs are typically too flexible to generate well-ordered crystals, Fabs must be generated through proteolytic cleavage, which is not required with recombinant Abs. For most labs, purification of the milligram quantities of recombinant Abs required for a crystallography campaign is more straightforward and reproducible compared to hybridomas-based expression and purification. Conformationally-specific Abs are easier to generate with recombinant approaches given the *in vitro* nature of the biopanning method making it possible to select for Abs in the presence of ligands or binding-partners. Recombinant Abs have been used extensively in GPRC structural biology making it possible to trap active states and

complexes with interaction partners[35,36]. Use of recombinant Abs is not restricted to membrane proteins as they have been used for co-crystallization of a number of soluble proteins including a module of the polyketide synthetase 6-deoxyethronolide B synthase[37] and matriptase[38,39]. To increase the utility of recombinant Abs for X-ray crystallography, recent work has been done to engineer the scaffold with desired properties, such as the use of 'elbow locking' mutations to rigidify the link between the constant and variable domains to increase crystallizability[40].

Recombinant antibodies in cryoEM

Recent advances in electron cryomicroscopy (cryoEM) have made it possible to solve near-atomic resolution structures of proteins[41]. While several well-behaved samples have achieved resolutions better than 2 Å, achieving the resolution required to build *de novo* models for new samples is still challenging[42]. Before the 'resolution-revolution', Abs were used as fiducial markers for EM by immunogold labeling[43] but more recently the use of recombinant Fabs as fiducial markers for single-particle cryoEM of small and challenging targets was demonstrated[44]. This technique has been used to determine a number of high resolution structures that were recalcitrant to high-resolution structure determination without a Fab [45,46]. Fabs have a number of advantages for this task. Unlike other methods of increasing molecular weight, such as green fluorescent protein or maltose-binding protein fusions[47], Fabs can specifically recognize and bind rigid three-dimensional epitopes thereby facilitating high-resolution refinement[44].

The characteristic shape of Fabs in both negative stain and cryoEM provides a means for assessing the quality of medium-low resolution structures in addition to high-resolution alignment[44]. As is the case with X-ray crystallography, recombinant Abs have also been crucial for the structure determination of several GPCR complexes[48–51], integrin[52], and ABC transporters[53] by trapping specific conformations. In addition to conformational selectivity, Fabs can alter the orientation distribution of vitrified samples. In the recent structure of TMEM16A, a calcium-activated chloride

channel, the sample in detergent had a significant preferred orientation bias resulting in a structure with anisotropic resolution[54]. By merging datasets with and without a Fab, it was possible to increase the resolution from 3.8 to 3.4 Å, as the two samples had different orientation distributions resulting in a final structure that was more isotropic and higher-resolution.

The low signal-to-noise ratio of cryoEM data makes refinement of psuedosymmetric complexes particularly challenging as protomers may not align properly if differences between them are small. Fabs have been used to overcome this problem in several systems as a symmetry-breaking fiducial mark. For example, Fabs against the heterodimeric ABC transporter TmrAB were used to increase the molecular weight of the relatively small membrane protein while simultaneously breaking a pseudo two-fold symmetry allowing for the unambiguous assignment of the individual protomers[55]. In the case of TmrAB, the estimated angular accuracy was significantly higher for the TmrAB-Fab complex relative to the apo sample. This same approach has been applied to several heteromeric ion channels[56,57]. Future engineering of antibody scaffolds may specifically tailor them to the unique requirements of single particle cryoEM with reduced flexibility and increased desired orientation distributions[58]. Since the theoretical minimum molecular weight required for high-resolution alignment is estimated to be around 50 kDa, approximately the same molecular weight of a Fab, it is conceivable that any Fab-antigen complex will be suitable for cryoEM in the future[59].

Conclusions

The lack of high-quality Abs for many macromolecules and their complexes limits our ability to determine protein structure, to detect proteins in pathology samples, and to image and treat diseases. The availability of potent, specific, reproducible, and readily renewable probes for the entire proteome, including hybridoma-refractory antigens, could transform the study of biology and

enable the discovery of new therapeutics. Recombinant antibody technology, in addition to existing hybridoma techniques, provides a robust pipeline for the generation of these essential reagents.

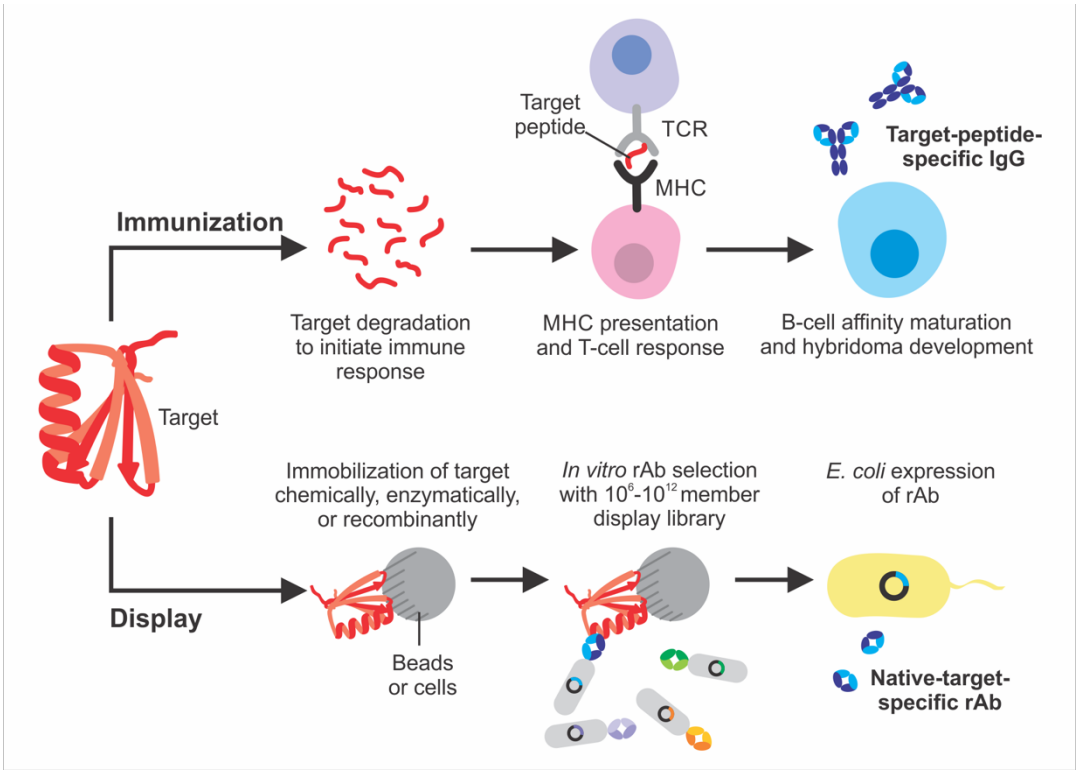

Figure 1.1: Antigen presentation in hybridoma antibody generation versus recombinant antibody display. Target antigen (red) follows hybridoma immunoglobulin G generation path (top) or recombinant antibody (rAb) generation path (bottom). In top path, the pink cell is a major histocompatibility complex (MHC) presenting cell, the purple cell is a T-cell, the blue cell is a B-cell, the black receptor is a MHC, and the grey receptor is a T-cell receptor (TCR). In bottom path, the grey oval particles are display library members (yeast or phage) with colored displayed rAb and the yellow cell is *Escherichia coli*.

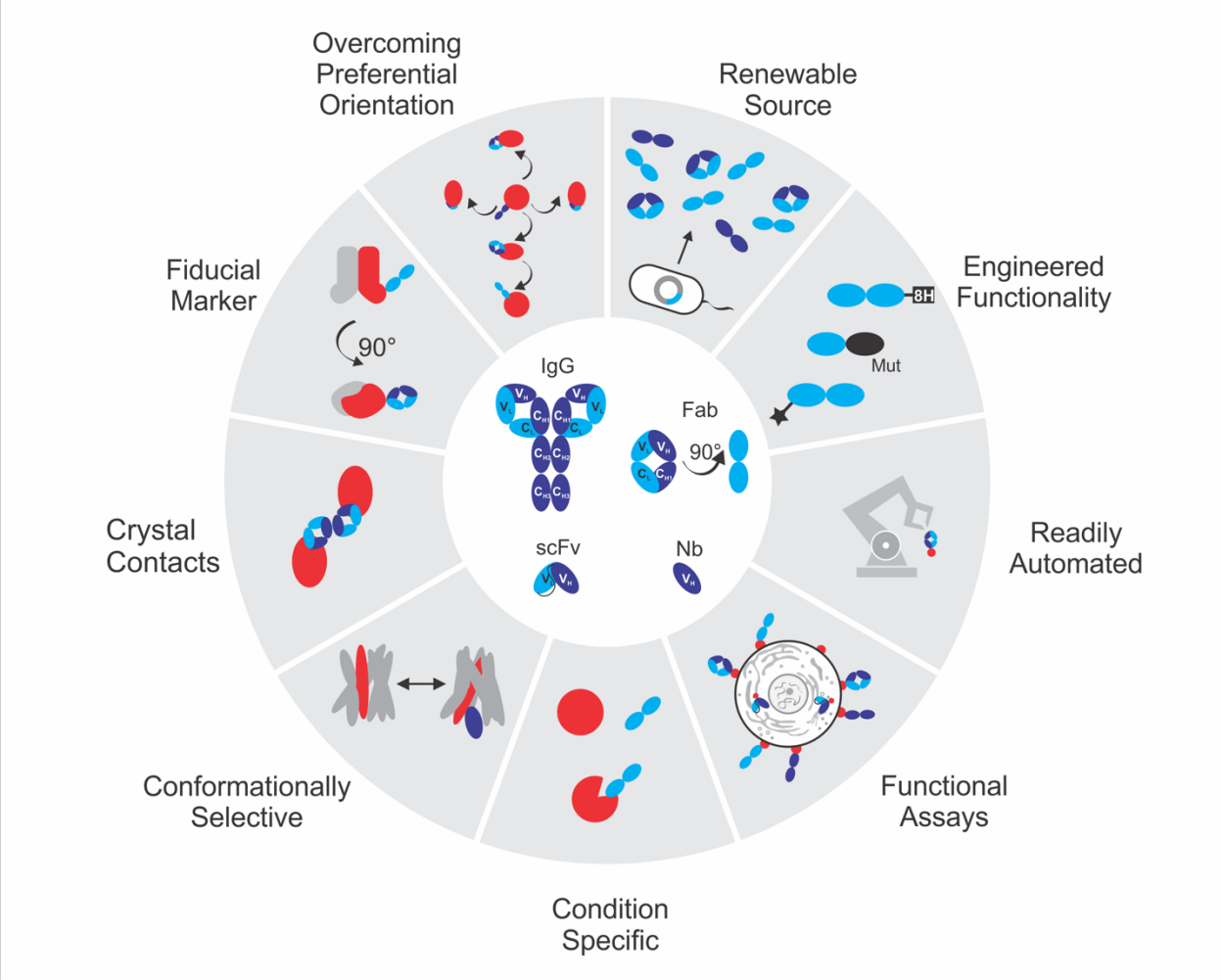

Figure 1.2: Different formats and important applications of recombinant antibodies.
Various antibody formats are shown in the center of the circle: immunoglobulin G (IgG), fragment of antigen-binding domain (Fab), single-chain variable fragment (scFv), and nanobody (Nb). IgGs are composed of two unique polypeptide chains, a heavy chain (H) and a light chain (L) based on their molecular weights. Each chain has one variable region (V_H, V_L). The light chain has one constant region (C_L) and the heavy chain has three constant regions (C_{H1-3}). Two heavy chains and two light chains come together to make an IgG. A Fab is composed of V_H, V_L, C_{H1} and C_L. An scFv is a single polypeptide chain composed of both V_H and V_L connected with a flexible linker. A Nb consists of only a V_H. Heavy chains are colored in dark blue, light chains are colored in cyan, and antibody targets are colored in red.

References

1. Kohler, G. & Milstein, C. Continuous cultures of fused cells secreting antibody of predefined specificity. *Nature* **256,** 495–497 (1975).
2. Clackson, T., Hoogenboom, H. R., Griffiths, A. D. & Winter, G. Making antibody fragments using phage display libraries. *Nature* **352,** 624–628 (1991).
3. Marks, J. D. *et al.* By-passing immunization. Human antibodies from V-gene libraries displayed on phage. *J. Mol. Biol.* **222,** 581–597 (1991).
4. Debs, B. E., Utharala, R., Balyasnikova, I. V., Griffiths, A. D. & Merten, C. A. Functional single-cell hybridoma screening using droplet-based microfluidics. *Proc. Natl. Acad. Sci.* **109,** 11570–11575 (2012).
5. Suter, L., Bruggen, J. & Sorg, C. Use of an enzyme-linked immunosorbent assay (elisa) for screening of hybridoma antibodies against cell surface antigens. *J Immunol Methods* **39,** 407–411 (1980).
6. Berek, C., Griffiths, G. M. & Milstein, C. Molecular events during maturation of the immune response to oxazolone. *Nature* **316,** 412–418 (1985).
7. Adamczyk, M., Gebler, J. C. & Wu, J. Papain digestion of different mouse IgG subclasses as studied by electrospray mass spectrometry. *J. Immunol. Methods* **237,** 95–104 (2000).
8. Colwill, K. *et al.* A roadmap to generate renewable protein binders to the human proteome. *Nat. Methods* **8,** 551–561 (2011).
9. Hoogenboom, H. R. *et al.* Antibody phage display technology and its applications. *Immunotechnology* **4,** 1–20 (1998).
10. Chao, G. *et al.* Isolating and engineering human antibodies using yeast surface display. *Nat. Protoc.* **1,** 755–768 (2006).

11. Pansri, P., Jaruseranee, N., Rangnoi, K., Kristensen, P. & Yamabhai, M. A compact phage display human scFv library for selection of antibodies to a wide variety of antigens. *BMC Biotechnol.* **9,** 1–16 (2009).

12. Fellouse, F. A. *et al.* High-throughput Generation of Synthetic Antibodies from Highly Functional Minimalist Phage-displayed Libraries. *J. Mol. Biol.* **373,** 924–940 (2007).

13. Haard, H. J. De *et al.* A Large Non-immunized Human Fab Fragment Phage Library That Permits Rapid Isolation and Kinetic Analysis of High Affinity Antibodies. *J. Biol. Chem.* **274,** 18218–18230 (1999).

14. McMahon, C. *et al.* Yeast surface display platform for rapid discovery of conformationally selective nanobodies. *Nat. Struct. Mol. Biol.* **25,** 289–296 (2018).

15. Bowley, D. R., Labrijn, A. F., Zwick, M. B. & Burton, D. R. Antigen selection from an HIV-1 immune antibody library displayed on yeast yields many novel antibodies compared to selection from the same library displayed on phage. *Protein Eng. Des. Sel.* **20,** 81–90 (2007).

16. Jones, M. L. *et al.* Targeting membrane proteins for antibody discovery using phage display. *Sci. Rep.* **6,** 26240 (2016).

17. Sun, J., Pons, J. & Craik, C. S. Potent and selective inhibition of membrane-type serine protease 1 by human single-chain antibodies. *Biochemistry* **42,** 892–900 (2003).

18. Hornsby, M. *et al.* A High Through-put Platform for Recombinant Antibodies to Folded Proteins. *Mol. Cell. Proteomics* **14,** 2833–2847 (2015).

19. Simmons, L. C. *et al.* Expression of full-length immunoglobulins in Escherichia coli: Rapid and efficient production of aglycosylated antibodies. *J. Immunol. Methods* **263,** 133–147 (2002).

20. Hawkins, R. E., Russell, S. J. & Winter, G. Selection of phage antibodies by binding affinity. Mimicking affinity maturation. *J. Mol. Biol.* **226,** 889–896 (1992).

21. Marks, J. D. *et al.* By-passing immunization: building high affinity human antibodies by chain shuffling. *Biotechnology. (N. Y).* **10,** 779–783 (1992).

22. Chaparro-Riggers, J. *et al.* Increasing serum half-life and extending cholesterol lowering in vivo by engineering antibody with pH-sensitive binding to PCSK9. *J. Biol. Chem.* **287,** 11090–11097 (2012).

23. Mould, D. R. & Meibohm, B. Drug Development of Therapeutic Monoclonal Antibodies. *BioDrugs* **30,** 275–293 (2016).

24. Redman, J. M., Hill, E. M., AlDeghaither, D. & Weiner, L. M. Mechanisms of action of therapeutic antibodies for cancer. *Mol. Immunol.* **67,** 28–45 (2015).

25. Lin, D. Y. *et al.* The PD-1/PD-L1 complex resembles the antigen-binding Fv domains of antibodies and T cell receptors. *Proc. Natl. Acad. Sci.* **105,** 3011–3016 (2008).

26. Balar, A. V. & Weber, J. S. PD-1 and PD-L1 antibodies in cancer: current status and future directions. *Cancer Immunol. Immunother.* **66,** 551–564 (2017).

27. Moroz, A. *et al.* A Preclinical Assessment of (89)Zr-atezolizumab Identifies a Requirement for Carrier Added Formulations Not Observed with (89)Zr-C4. *Bioconjug. Chem.* **29,** 3476–3482 (2018).

28. LeBeau, A. M. *et al.* Imaging a functional tumorigenic biomarker in the transformed epithelium. *Proc. Natl. Acad. Sci. U. S. A.* **110,** 93–98 (2013).

29. Ghosh, E. *et al.* A synthetic intrabody-based selective and generic inhibitor of GPCR endocytosis. *Nat. Nanotechnol.* **12,** 1190–1198 (2017).

30. Binning, J. M. *et al.* Fab-based inhibitors reveal ubiquitin independent functions for HIV

Vif neutralization of APOBEC3 restriction factors. *PLoS Pathog.* **14,** e1006830 (2018).

31. Pollock, S. B. *et al.* Highly multiplexed and quantitative cell-surface protein profiling using genetically barcoded antibodies. *Proc. Natl. Acad. Sci. U. S. A.* **115,** 2836–2841 (2018).

32. Carpenter, E. P., Beis, K., Cameron, A. D. & Iwata, S. Overcoming the challenges of membrane protein crystallography. *Curr. Opin. Struct. Biol.* **18,** 581–586 (2008).

33. Ostermeier Christian, Iwata So, Ludwig Bernd, M. H. Fv fragment-mediated crystallization of the membrane protein bacterial cytochrome c oxidase. *Nature* **2,** 983–989 (1995).

34. Zhou, Y., Morais-Cabral, J. H., Kaufman, A. & MacKinnon, R. Chemistry of ion coordination and hydration revealed by a K+ channel-Fab complex at 2.0 A resolution. *Nature* **414,** 43–48 (2001).

35. Rasmussen, S. G. *et al.* Crystal structure of the human β2 adrenergic G-protein-coupled receptor. *Nature* **450,** 383–387 (2007).

36. Rasmussen, S. G. F. *et al.* Structure of a nanobody-stabilized active state of the β2adrenoceptor. *Nature* **469,** 175–181 (2011).

37. Li, X. *et al.* Structure-Function Analysis of the Extended Conformation of a Polyketide Synthase Module. *J. Am. Chem. Soc.* **140,** 6518–6521 (2018).

38. Schneider, E. L. *et al.* A reverse binding motif that contributes to specific protease inhibition by antibodies. *J. Mol. Biol.* **415,** 699–715 (2012).

39. Farady, C. J., Egea, P. F., Schneider, E. L., Darragh, M. R. & Craik, C. S. Structure of an Fab-Protease Complex Reveals a Highly Specific Non-canonical Mechanism of Inhibition. *J. Mol. Biol.* **380,** 351–360 (2008).

40. Bailey, L. J. *et al.* Locking the Elbow: Improved Antibody Fab Fragments as Chaperones for Structure Determination. *J. Mol. Biol.* **430,** 337–347 (2017).

41. Cheng, Y. Single-particle Cryo-EM at crystallographic resolution. *Cell* **161,** 450–457 (2015).

42. Bartesaghi, A. *et al.* Atomic Resolution Cryo-EM Structure of β-Galactosidase. *Structure* **26,** 848–856.e3 (2018).

43. Faulk, W. P. & Taylor, G. M. An immunocolloid method for the electron microscope. *Immunochemistry* **8,** 1081–1083 (1971).

44. Wu, S. *et al.* Fabs enable single particle cryoEM studies of small proteins. *Structure* **20,** 582–592 (2012).

45. Kintzer, A. F. *et al.* The structural basis for activation of voltage sensor domains in an ion channel TPC1. *Proc Natl Acad Sci U S A* **115,** E9095–E9104 (2018).

46. Butterwick, J. A. *et al.* Cryo-EM structure of the insect olfactory receptor Orco. *Nature* **560,** 447–452 (2018).

47. Coscia, F. *et al.* Fusion to a homo-oligomeric scaffold allows cryo-EM analysis of a small protein. *Sci. Rep.* **6,** 1–11 (2016).

48. Liang, Y. L. *et al.* Phase-plate cryo-EM structure of a biased agonistbound human GLP-1 receptor-Gs complex. *Nature* **555,** 121–125 (2018).

49. Liang, Y. L. *et al.* Phase-plate cryo-EM structure of a class B GPCR-G-protein complex. *Nature* **546,** 118–123 (2017).

50. Zhang, Y. *et al.* Cryo-EM structure of the activated GLP-1 receptor in complex with a G protein. *Nature* **546,** 248–253 (2017).

51. Kang, Y. *et al.* Cryo-EM structure of human rhodopsin bound to an inhibitory G protein.

Nature **558,** 553–558 (2018).

52. Cormier, A. *et al.* Cryo-EM structure of the αvβ8 integrin reveals a mechanism for stabilizing integrin extension. *Nat. Struct. Mol. Biol.* **25,** (2018).

53. Taylor, N. M. I. *et al.* Structure of the human multidrug transporter ABCG2. *Nature* **546,** 504–509 (2017).

54. Dang, S. *et al.* Cryo-EM structures of the TMEM16A calcium activated chloride channel. *Nature* **552,** 426–429 (2017).

55. Kim, J. *et al.* Subnanometre-resolution electron cryomicroscopy structure of a heterodimeric ABC exporter. *Nature* **517,** 396–400 (2015).

56. Lü, W., Du, J., Goehring, A. & Gouaux, E. Cryo-EM structures of the triheteromeric NMDA receptor and its allosteric modulation. *Science.* **355,** 1–9 (2017).

57. Zhu, S. *et al.* Structure of a human synaptic GABAA receptor. *Nature* **559,** 67–72 (2018).

58. Liu, Y., Gonen, S., Gonen, T. & Yeates, T. O. Near-atomic cryo-EM imaging of a small protein displayed on a designed scaffolding system. *Proc. Natl. Acad. Sci.* **115,** 3362–3367 (2018).

59. Rosenthal, P. B. & Henderson, R. Optimal determination of particle orientation, absolute hand, and contrast loss in single-particle electron cryomicroscopy. *J. Mol. Biol.* **333,** 721–745 (2003).

Chapter 2

The structural basis for activation of voltage sensor domains in an ion channel TPC1

Contributing Authors

Alexander F. Kintzer†,[1], Evan M. Green†,[1], Pawel K. Dominik†,[1,2], Michael Bridges[3], Jean-Paul Armache[1], Dawid Deneka[2], Sangwoo S. Kim[2], Wayne Hubbell[3], Anthony A. Kossiakoff[2], Yifan Cheng*,[1,4], and Robert M. Stroud*,[1]

[1]University of California, San Francisco, Department of Biochemistry and Biophysics

[2]University of Chicago, Department of Biochemistry and Molecular Biology

[3]University of California, Los Angeles, Jules Stein Eye Institute and Department of Chemistry and Biochemistry

[4]Howard Hughes Medical Institute

†These authors contributed equally to this work

Abstract

Voltage sensing domains (VSDs) couple changes in transmembrane electrical potential to conformational changes that regulate ion conductance through a central channel. Positively charged amino acids inside each sensor cooperatively respond to changes in voltage. Our previous structure of a TPC1 channel captured the first example of a resting-state VSD in an intact ion channel. To generate an activated state VSD in the same channel we removed the lumenal inhibitory Ca^{2+}-binding site (Ca_i^{2+}), that shifts voltage-dependent opening to more negative voltage and activation at 0 mV. Cryo-EM reveals two coexisting structures of the VSD, an intermediate state 1 that partially closes access to the cytoplasmic side, but remains occluded on the lumenal side and an intermediate activated state 2 in which the cytoplasmic solvent access to the gating charges closes, while lumenal access partially opens. Activation can be thought of as moving a hydrophobic insulating region of the VSD from the external side, to an alternate grouping on the internal side. This effectively moves the gating charges from the inside potential to that of the outside. Activation also requires binding of Ca^{2+} to a cytoplasmic site (Ca_a^{2+}). An X-ray structure with Ca_a^{2+} removed and a near-atomic resolution cryo-EM structure with Ca_i^{2+} removed define how dramatic conformational changes in the cytoplasmic domains may communicate with the VSD during activation. Together four structures provide a basis for understanding the voltage dependent transition from resting to activated state, the tuning of VSD by thermodynamic stability, and this channel's requirement of cytoplasmic Ca^{2+}-ions for activation.

Introduction

Voltage sensing domains (VSDs) are four-helical bundle domains, termed S1-S4 that respond to changes in membrane potential by allowing 'gating' charges, generally positively charged arginine or occasionally lysine side chains in the fourth transmembrane helix S4 (charges referred to as R1-R5) to move relative to a charge-transfer center (CT) [1,2] that contains counter charges in the surrounding helices S1-S3 and an aromatic residue (Y, F) that seals the VSD to solvent passage.

The number of gating charges in each VSD that move across the membrane from connection to the cytoplasmic side to the extracellular (or lumenal) side during activation is typically measured as 2-3 and up to 5 positive charges. The basis for structural and electrical changes in S4 that give rise to voltage-dependence is key to understanding the response of voltage-gated ion channels to changes in membrane potential.

In voltage-gated ion channels, the movement of S4 is connected via an S4-S5 linker helix on the cytoplasmic side to the pore helices S5-S6 of the ion channel, and also through Van der Waals hydrophobic contacts between S4 and the pore-forming domains. In excitable cells, activation of the VSD in response to membrane depolarization greatly increases the probability of channel opening[3,4].

Several models have been proposed for voltage-dependent activation. The 'Sliding Helix'[5], 'Rotating helix'[6,7], and 'Paddle'[8] models suggest that S4 moves substantially (vertically or in rotation) in the membrane to translate the gating charges across the membrane (SI Appendix, Fig. S1). In Sliding Helix and Rotating Helix models, the gating charges interact with counter anions or aqueous environments to avoid the energetic penalty of placing a charge in a hydrophobic environment. Lanthanide-based resonance energy transfer measurements suggest

that gating charges do not move extensively during activation, but rather achieve alternating exposure to the internal and external milieu through conformational changes in the VSD helices S1-S4 [9]. A 'ratchet' model also includes the possibility of multiple intermediate states of S4[10]. Electrophysiology, electron paramagnetic resonance (EPR) spectroscopy, X-ray structures, disulfide crosslinking, and simulations support a combination of translation and rotation of S4 during activation [11–18]. No structural information until now exists for voltage-gated channels captured in multiple activation states, precluding an atomic scale evaluation of the mechanism of voltage-dependent changes, or how they translate to channel activation. Our previous crystal structure of wild-type *Arabidopsis thaliana* two-pore channel 1 ($AtTPC1_{WT}$) provided the first resting-closed state in an intact ion channel[19,20], the electrophysiological state that forms under high lumenal 1 mM (>100μM) Ca^{2+}-ion concentration. Here we sought to determine structures for the activated-state of AtTPC1 that is formed in low lumenal (<100μM) Ca^{2+}-ions by removing the inhibitory lumenal Ca^{2+}-binding site in VSD2 (Ca_i^{2+}), while keeping the cytoplasmic activation site (Ca_a^{2+}) occupied with >300μM cytoplasmic Ca^{2+}-ions [21]. Secondly, we wanted to determine the mechanism for the channel's requirement of cytoplasmic Ca^{2+}-ions for activation by removing the Ca_a^{2+} site.

TPCs are a family of ion channels that regulate ion conductance across endolysosomal membranes[22,23,21]. Located in endosomes that endocytose from the plasma membrane, initially with ~1mM extracellular Ca^{2+} concentration, they regulate the conductance of Na^+- and/or Ca^{2+}-ions out of the endolysosome, intravesicular pH [24], trafficking [25], and membrane excitability [26]. Cytoplasmic Ca^{2+}-ions (>300 μM) are required for any activation of AtTPC1 [27], whereas lumenal Ca^{2+}-ions (>100 μM) suppress voltage-dependent activation [20,28]. TPCs encode two pore-forming domains on a single chain with two non-equivalent VSDs (S1-S4, S7-S10) and

pore helices (S5-S6, S11-S12). In AtTPC1 only VSD2s (S7-S10) respond to changes in voltage [20]. Three arginines on S10 of each VSD2 (equivalent to S4 in the VSD of tetrameric ion channels) in AtTPC1 are required for voltage-dependent activation. A homo-dimer of two TPCs forms the central functional channel surrounded by four pore-forming domains.
The dependence of AtTPC1 on external and internal Ca^{2+} offer the opportunity to visualize the resting state of a voltage sensing domain of an intact channel, and the activated state and to ask how voltage changes are detected and relayed.

Lumenal Ca^{2+}-ions suppress activation of AtTPC1 via binding to Ca_i^{2+} located in the active voltage sensor VSD2 with EC_{50} ~0.1mM. This previously enabled trapping of the resting-state VSD2 of wild-type AtTPC1 by including 1 mM Ca^{2+}-ions [19,20]. Replacement of the Ca^{2+}-chelating amino acids by mutagenesis (D240N, D454N, E528Q; termed $AtTPC1_{DDE}$) shifts voltage-dependent activation by -50 mV, such that the channel is open at 0 mV [20,28] and VSD2 in an activated conformation. Using $AtTPC1_{DDE}$ we sought to determine the structure of an activated state of the same intact channel where we had previously determined a resting state.

Channel opening requires Ca^{2+}-ion binding to Ca_a^{2+} mediated by D376 of cytoplasmic EF-hand domain helix 3-4 loop (EF3-EF4). Removal of cytoplasmic Ca^{2+}-ions or the mutation D376A ($AtTPC1_{DA}$) yields permanently closed channels [29]. The absolute requirement of the Ca_a^{2+} site for voltage-dependent activation led us to hypothesize that channel activation depends on communication between Ca_a^{2+} and VSD2 [21]. Using the D376A mutation we sought to determine how cytoplasmic Ca^{2+} evokes activation.

Results and Discussion

Cryo-EM structures of AtTPC1$_{DDE}$

As a basis for understanding the voltage-dependent activation mechanism and its modulation by Ca^{2+}-ions, we determined the structure of AtTPC1$_{DDE}$ by cryo-EM (Figure 1a and SI Appendix, Fig. S2, Fig. S3, Fig. S4, Table S1). We employed saposin A nanoparticles [30] to reconstitute AtTPC1$_{DDE}$ into a membrane environment, and an antibody Fab made against AtTPC1 (CAT06/H12) [31] to facilitate particle alignment [32] (SI Appendix, Fig. S5, Fig. S6, SI Discussion).

With a nominal resolution of 3.3 Å, the density map of AtTPC1$_{DDE}$ is of high quality (SI Appendix, Fig. S4a), allowing additional *de-novo* interpretation of the AtTPC1 N-terminal domain (NTD), the S1-S2 linker, EF3-EF4 with an intact Ca_a^{2+} site, the upper vestibule of the pore, and the C-terminal domain (CTD). Three ions lie in the selectivity filter, consistent with previously defined Ca^{2+}/Na^{+}-binding sites [19,20,33]. Fourteen lipid molecules surround the channel in the lumenal leaflet with two on the cytoplasmic side (SI Appendix, Fig. S7). S1-S6 are well defined and remain stationary between all of the AtTPC1 structures. In AtTPC1$_{DDE}$, major rearrangements are observed in the VSD2, the upper vestibule of pore, and EF3-EF4 on the cytoplasmic side, relative to AtTPC1$_{WT}$ (Figure 1b). The position of three residues known to be phosphorylated (S22, T26, and T29) are observed in previously unresolved portions of the NTD (SI Appendix, Fig. S4a, SI Discussion) [19].

The Fab binds to the EF1-EF2 loop, EF4, and S6 on the cytoplasmic side. The Fab binding affinity is the same with and without Ca^{2+} ions, in other molecular conditions tested (1 mM EGTA, 1 μM trans-NED19, 1 μM Nicotinic Acid Adenine Dinucleotide Phosphate), and in three different constructs (AtTPC1$_{WT}$, AtTPC1$_{DDE}$, AtTPC1$_{DA}$), indicating that the Fab binding

does not distinguish between nor is likely to influence the activation state (SI Appendix, Fig. S5c-d). Most of the variable domain of the Fab is visible, allowing interpretation of the AtTPC1$_{DDE}$-Fab interface (SI Appendix, Fig. S6e-f). The constant domain of the Fab is flexible and not resolved to high resolution.

Activation of the voltage sensor

Lumenal Ca^{2+}-ions inhibit AtTPC1 channel activation half maximally at ~0.1 mM concentration[20] via binding to Ca_i^{2+} [21] between VSD2 (D454 in the S7-S8 loop, and E528 in S10), and the pore (D240). D454N, also named *fou2* (fatty acid oxygenation up-regulated 2) [28], abolishes inhibition by lumenal Ca^{2+}-ions, increasing channel open probability by shifting the voltage-dependent channel opening towards more hyperpolarizing potentials [28,20]. Ca^{2+}-ions do not inhibit AtTPC1$_{DDE}$ at 1 mM and up to 10 mM [33]. Thus, the Ca_i^{2+} site is functionally abolished in AtTPC1$_{DDE}$ under cryo-EM conditions and thereby mimics the activated state under voltage and low lumenal Ca^{2+}-ion conditions [20,33].

While the overall resolution of AtTPC1$_{DDE}$ is excellent, density for S7-S10 of VSD2 is significantly weaker indicating conformational heterogeneity. Focused classification identified two states of VSD2, each with an overall resolution of 3.7 Å, but with distinct and different conformations of the S7-S10 domain structure (state 1 and 2) (SI Appendix, Table S1, Fig. S3, See Methods). We therefore conclude that these two conformations represent different functional states of the AtTPC1$_{DDE}$ channel. They suggest a model for the voltage-activation of AtTPC1, and a mechanism for dependence on lumenal Ca^{2+}-ions.

To confirm that the structural rearrangements in VSD2 were not induced by saposin A we determined a ~7Å reconstruction of AtTPC1$_{WT}$ in both detergent and in saposin A. In these the

overall channel architecture is comparable to the $AtTPC1_{WT}$ crystal structure (SI Appendix, Fig. S8).

The local resolution of VSD2 (S7-S10) ranges from 4-6 Å in both states, making it possible to model the intermediate active state of VSD2 based on the 2.8 Å X-ray structure of $AtTPC1_{WT}$ (SI Appendix, Fig. S4b, c, See Methods under Structure Determination and Refinement)[19]. Atomic structures for states 1 and 2 were determined by real-space and B-factor refinement against the cryo-EM densities. Changes in solvent accessibility at the lumenal and cytoplasmic boundaries of VSD2 were apparent from the comparison of these new structures of AtTPC1 and the previous resting-state. Taking the resting state structure of $AtTPC1_{WT}$ as a reference (PDBID 5DDQ; ref. [19]), transmembrane helices S7-S10 in state 1 rotate in a counterclockwise manner with respect to $AtTPC1_{WT}$ (Figure 2). The helices twist to partially close the cytoplasmic solvent access to the gating charges of VSD2 (Figure 3), while the lumenal face remains occluded. Among all helices of VSD2, the key arginine-rich S10 has the least movement, and R537 (R1) remains interacting with the CT (Y475), albeit the changes in S8 conformation place R1 on the opposite horizontal face of the CT as compared with $AtTPC1_{WT}$. S8 moves upward in the membrane plane by nearly one helical turn, thus moving the CT into place to interact with R1 in similar manner to $AtTPC1_{WT}$. State 1 probably represents a resting-state structure present in low lumenal (<0.1 mM) Ca^{2+}-ion concentrations.

In state 2, VSD2 rotates ~20˚ clockwise in the plane of the membrane with respect to $AtTPC1_{WT}$ (Figure 2). Helices S7-S10 reorient dramatically leading to an opening of the lumenal face of VSD2 (Figure 3). Tilting of S10 and rotation of S8 around S10 moves the CT downward, placing R1 in an activated conformation. The cytoplasmic face is fully closed in state 2 while the

lumenal side is partially open. VSD2 has effectively alternated solvent access, or electrical contact from the cytoplasmic to the lumenal side of the membrane.

Clockwise rotation was proposed to connect resting- and active-state conformations on the basis of comparing previous voltage-gated channel structures [13,19,34]. During review of this manuscript, activated state structures of mouse TPC1 were determined [35]. Comparing the activated-state mouse TPC1 to resting- and intermediate-state AtTPC1 supports the proposed role of VSD2 rotation during channel activation. The observation of clockwise rotation in multiple activated-state structures supports our conclusion that state 2 represents an intermediate-activated state of AtTPC1.

These two states of VSD2 in AtTPC1 are likely to represent structures that VSD2 adopts in low lumenal Ca^{2+} during activation. The overall movement of VSD2 during activation serves to dilate the lumenal face of VSD2, close off the cytoplasmic leaflet to solvent, and move the CT below a gating charge in the membrane. This would reconnect the positive gating charges from the potential of the cytoplasmic side to the potential of the lumenal side upon activation, mediated by tilt and twisting of S7, S8, S9 around S10. This is all that is necessary to transport the gating charge arginine residues from cytoplasmic electrical connection, to the external potential. A hydrophobic sealed region between all four helices forms a thin outer insulating layer in the resting state, while in the activated state this becomes open to solvent and the bundle twists to form a hydrophobic insulating region closer to the cytoplasmic side.

Drug and Lipid Binding Sites

The high resolution map enabled refinement of a total of 14 lipids on the lumenal and 2 on the cytoplasmic leaflet of the membrane. The lumenal lipids are modeled as the 16-carbon

containing palmitic acid, the predominant lipid length in soy polar lipids, whereas the cytoplasmic lipids are modeled as 18-carbon phosphatidic acid (PA). 12 lipids bind to the long axis of AtTPC1, occupying the binding site for Ned19 (SI Appendix, Fig. S7, ref. [19,21]). Ned19 binding may disrupt these structured lipids, acting as a steric block to prevent S7 and pore movements during gating. One lipid binds to a buried site along the short axis, sandwiched in between the pore domains. Based on homology to Ca_v channels in this region and recent structures of bacterial Ca_v channels (Ca_vAb) bound to dihydropyridines (DHP) (amlodipine and nimodipine) and PPA (verapamil) inhibitors[36], the short axis in transmembrane segments S6 and S12 is a likely site for binding of Tetrandrine, a bis-benzylisoquinoline alkaloid isolated from the Chinese herb *Stephania tetrandra* and approved medications of the DHP class of L-type Ca_v antagonists–all TPC channel blockers.

The lumenal PA lipids bind along the short axis in a pocket formed by S1 of VSD1, the S10-S11 linker, S11, and the S8-S9 linker of VSD2. The alkyl chains make Van der Waals interactions, whereas the phosphoglycerol headgroup makes hydrogen bonds to the backbone of W492 and to the sidechain of R498 and S8-S9 of VSD2. The S8-S9 linker moves 4Å inward in the $AtTPC1_{DDE}$ structure to form the PA binding site, which would not be intact in the $AtTPC1_{WT}$ resting-state. Therefore, this lipid binding site is likely specific for $AtTPC1_{DDE}$. Certain lipids may occupy this site during activation of AtTPC1. Polyunsaturated fatty acids inhibit plant TPC1 activation, but the binding site has not been determined (38). In principle, polyunsaturated fatty acids could mimic the observed site in the resting-state and prevent activation.

Charge transfer mechanism

State 2 represents an intermediate activation state of VSD2 where the gating charge R1 is transferred across the membrane (Figure 3). In this state, the CT moves downwards, R1 moves slightly upwards, and overall the VSD2 bundle rotates by ~20˚ in the membrane plane with respect to the adjacent pore domains. In this the voltage-sensing helix S10 pivots only 2-3˚ inward toward the pore. Importantly, the three observed states of the VSD thus far are not related by rigid-body rotations. These changes in VSD2 make R1 more accessible to solvent on the lumenal side while charges R2 and R3 are shielded from access to the cytoplasmic side; there is a net transfer of charge from cytoplasmic side (in the resting state) to the outside (in the activated state).

Pore conformational changes

High-resolution density for the pore defines the consequences of activation by removal of the external Ca_i^{2+} site on VSD2 on the central channel (Figure 4a, b). As a consequence of the rearrangement of VSD2 the upper vestibule and the upper selectivity filter of the channel open along the ion permeation pathway (Figure 4c), while the lower gate remains closed (Figure 4d). Full channel opening may be evoked by passage of ions or an additional energy barrier, because electrophysiological studies show the channel is maximally open at 0 mV with removal of the Ca_i^{2+} site.

In the selectivity filter, three ions are observed (Figure 4e, f). Site 1 and 3 were occupied by Ca^{2+} mimetics, Yb^{3+} or Ba^{2+}, in $AtTPC1_{WT}$ structures (19, 20). Site 2 was seen to be occupied by Na^+ in the Na^+-selective chimera of AtTPC1(33). Since $AtTPC1_{DDE}$ contains 1 mM Ca^{2+} and the channel is Ca^{2+}-selective, these are probably hydrated Ca^{2+}-ions (SI Appendix, Discussion).

Sidechain interactions from the upper vestibule of S11-S12 exclusively coordinate site 1. The side chains of D606 move inward to coordinate site 1 with E605 (Figure 4g). E605-Ca^{2+} (5.5 Å) and D606-Ca^{2+} (4.6 Å) distances are consistent with the radius of a hydrated Ca^{2+} ion. There are readjustments throughout the channel suggesting that VSD2 activation by removal of the lumenal Ca_i^{2+} site can indeed potentiate channel opening as observed by electrophysiology.

The observation of upper and lower selectivity filter and activation gate operating independently in our structures suggests a multi-step gating mechanism that resembles that proposed for TRPV1 channel activation (39). Activation of the VSDs could lead to opening of the selectivity filter and activation gate in two steps. First, the upper selectivity filter opens in response to rotational rearrangement and partial activation of the VSDs, then the lower selectivity filter and activation gate open when the VSD achieves maximal activation.

Cytoplasmic activation by Ca^{2+}-ions

Full voltage-dependent activation of AtTPC1 requires ~0.3 mM cytoplasmic Ca^{2+} evoked by Ca^{2+}-binding to the EF3-EF4 loop (20, 29). D376 in EF3 is critical; when substituted D376A in $AtTPC1_{DA}$ the channel remains closed and is no longer responsive to membrane potential (29). We determined the crystal structure of $AtTPC1_{DA}$ (Figure 5a, Table S2) to 3.5 Å resolution by X-ray crystallography. When compared with the $AtTPC1_{WT}$ crystal structure, removing the activating cytoplasmic Ca_a^{2+} binding site leads to higher dynamic motion (B-factors) not only in the EF-hand and the CTD, but also in the VSDs and upper vestibule of the pore, showing that the activating cytoplasmic site may act through effects on the VSDs (SI Appendix, Discussion).

$AtTPC1_{DA}$ is in a resting-state as expected. However, there is an overall effect of increasing the dynamical motion of VSD1, VSD2 and the pore (in the context of otherwise

identical overall B-factors), showing that Ca_a^{2+} has an allosteric effect in stabilization that could impact voltage dependence (VSDs) and conductance (the pore). The regions of increased motion in $AtTPC1_{DA}$ correspond to the regions that undergo conformational change in $AtTPC1_{DDE}$, suggesting that there is a pathway for coupling cytoplasmic activation at Ca_a^{2+} to voltage dependence of activation in VSD2 and transmission to the pore.

The Ca_a^{2+} site in EF3 is fully formed in the cryo-EM structure of $AtTPC1_{DDE}$, whereas it was partially occupied in $AtTPC1_{WT}$ and was in a more extended conformation(19, 20) (Figure 5b). In $AtTPC1_{DDE}$, EF3 alone lies 7 Å closer to the transmembrane domain and rotates 20° to make close contacts with EF4 (Figure 5c). The Ca_a^{2+}chelating residues E374, D376, and D380 order the EF3-EF4 loop around the activating Ca_a^{2+} site (Figure 5c). Movement of EF3 leaves the EF1-EF2 Ca^{2+} site unaltered. Therefore, EF3 is capable of undergoing large-scale movements that change the structure of the cytoplasmic domains and their connection to VSD2, suggesting that activation on the cytoplasmic side can act reciprocally through VSD2.

The conformation of the cytoplasmic domains seen in $AtTPC1_{DDE}$, probably reflects the predominant structure in $AtTPC1_{WT}$ (rather than the crystal structure) because the conformation of EF3 is conserved in cryo-EM structures from several conditions; detergent and saposin A nanoparticles of $AtTPC1_{WT}$, and $AtTPC1_{DDE}$, and when bound to either of two different Fab molecules (SI Appendix, Fig. S8c).

The CTD of AtTPC1 is indispensable for channel activation(40). Removal or truncation by 29 residues abolishes channel function. In the crystal structure of $AtTPC1_{WT}$, the CTD forms an intramolecular complex with the EF3 via salt-bridge interaction D376-R700, leading to the hypothesis that the EF3-CTD complex could undergo conformational changes upon activating cytoplasmic Ca^{2+}-binding (19). In the cryo-EM structures the CTD moves toward the membrane

vertically by 13Å to accommodate the upward movement of EF3 upon forming the cytoplasmic activating Ca_a^{2+} site (Figure 5b). The salt-bridge (D376-R700) that previously linked the CTD to EF3 in $AtTPC1_{WT}$ breaks to allow D376 to chelate the Ca_a^{2+} site. This can explain why only substitution of D376 and not the other chelating residues abolishes Ca^{2+}-activation(29). In $AtTPC1_{DDE}$, the CTD now forms a hydrogen bond (E366-E694) with EF3 and hydrogen bonds (N697-I371) via the backbone (Figure 5d). Following the interaction with EF3, and a β-turn the CTD to folds back on itself to form a charged zippered interaction (R696-D691, R700-Q688, R707-E684) between the signal poly-R and poly-E motifs of the CTD (19). The poly-E motif connects directly to the pore gate (Figure 5e). The role of the CTD on channel activation may be to stabilize the EF3 helix in both apo- and Ca^{2+}-bound conformations to allow communication of EF3 movement to VSD2 and the pore gate. Upon removal of Ca^{2+}, the CTD could adopt an extended conformation to reform the salt-bridge interaction D376-R700 with EF3. Without the CTD, EF3 may not be able to reform the Ca_a^{2+} site and would become trapped in an inactive state.

To further investigate the conformation of EF3 in solution, we performed continuous wave electron paramagnetic resonance (CW-EPR) experiments using spin-labeled full-length AtTPC1 lacking cysteines ($AtTPC1_{cysless}$; See Methods) in detergent micelles. Ten positions in the CTD, gate, and EF-hand domains were examined by spin-probe mobility and responsiveness to Ca^{2+}-ions. Labeling at a site on EF3 (R379) indicates a conformational shift to higher probe mobility as compared with EGTA, indicating that the probe changes environment in the presence of Ca^{2+}-ions (SI Appendix, Fig. S9). Mutation of the Ca_a^{2+} site but not the Ca^{2+}-site in EF1-EF2 abolishes the Ca^{2+}-dependent increase in probe mobility, suggesting that EF3/Ca_a^{2+} changes conformation upon increasing cytoplasmic Ca^{2+}-ion concentrations. The data suggest that the

$AtTPC1_{WT}$ crystal structure likely represents an apo-state of EF3, whereas $AtTPC1_{DDE}$ represents a Ca^{2+}-bound conformation present along the pathway of activation.

Alternate Access Mechanism of Activation

As the electric potential changes across a membrane, functional voltage sensors find a new free energy minimum. Under hyperpolarizing conditions, the favorable electrostatic free energy component of positive gating charges' attraction to internal negative potential is balanced against a structural 'distortion' free energy cost. Depolarization therefore releases both of these components to populate a new overall equilibrium state that includes a component that regulates the open probability of the pore. Release of the electrostatic free energy is achieved by alternating access of the positively charged gating charges on S10 to solvent from the cytoplasmic side in the hyperpolarized resting state, to a state in which they are insulated from the cytoplasmic side, and become accessible to solvent from the lumenal side, without any necessity for vertical movement of the gating charges themselves. The structures of $AtTPC1_{WT}$ and $AtTPC1_{DDE}$ suggest that this 'alternating access' mechanism plays the key role. The movement of the VSD2 helices S7, S8, S9 with respect to the gating charges on S10 achieve this (Figure 6).

Hence the potential gradient is focused across a thin hydrophobic region close to the lumenal (external) side in the resting-state, and alternately across one on the cytoplasmic side in the activated-state. Thus, the gating charges do not require any vertical movement across the bilayer as the electrically insulating region, which includes the CT and across which the voltage gradient is formed, moves from outside of the gating charges in the resting-state voltage sensor,

to the cytoplasmic side of gating charges in the activated-state. Thus, the electric component of free energy is released.

The mechanism is unique versus most previously proposed models in that S7-S9, not only S10 that is closest to the pore, are crucial during voltage-activation to move gating charges from the electric potential on one side of the membrane to the potential of the other side without any necessary vertical translation of S10. Even after this major driving effect, gating charge side chains will also readjust in context of their different environments and some vertical movement may find more favorable energetics in the shallow energy gradient around them.

There is a teleologically favorable aspect to this alternate access mechanism in that it does not need to remove any hydrophobic residues out of the bilayer as would be required of a model involving large vertical movement of S10. It also does not need to rebuild the hydrophobic interface between S10 of the VSD and the walls of the pore with which it forms the primary contact that may be important in changes that alter open probability of the channel. Simulations of VSDs that assume a linear gradient of electric potential across the bilayer that changes only in slope on depolarization, but not position of start and end points across the VSD may not represent the true physiological state.

The Gibbs free energy change on moving one charge across a transmembrane potential difference of -70 mV is -1.6 kcal/mole. The measured gating charge transfer for activation of AtTPC1 is 3.9 charges(20) or -6.3 kcal/mole in free energy difference. Ca^{2+} binding to the lumenal Ca_i^{2+} site effectively stabilizes the resting-state. The EC_{50} for the Ca_i^{2+} site is ~0.1 mM. Therefore, assuming a K_d ~0.1 mM, the free energy released by removing each Ca_i^{2+} site is ~5.6 kcal/mole per site (or ~11.2 kcal/mole per AtTPC1 channel). It is not unreasonable that this difference, in releasing the restraint at Ca_i^{2+}, could allow the VSD to reach its active state that

would normally be evoked by depolarizing the transmembrane potential at low lumenal Ca^{2+}. The fact that we observe intermediate states of TPC1 upon removing Ca_i^{2+} rather than the fully activated state suggests that the membrane voltage, or the passage of ions may contribute additional energy to maximize activation of VSD2 and channel open probability.

The mechanism suggested for AtTPC1 voltage dependent activation is the first time that atomic structures have been determined for intermediates on transition from resting-state to activated-state in an intact voltage-dependent channel. The structures also capture large-scale rotation of VSDs that could play a role in activation. It could be a general way in which gating charge can move energetically downhill in response to a change in voltage, without the energetic cost of removing any hydrophobic lipophilic regions out of the membrane.

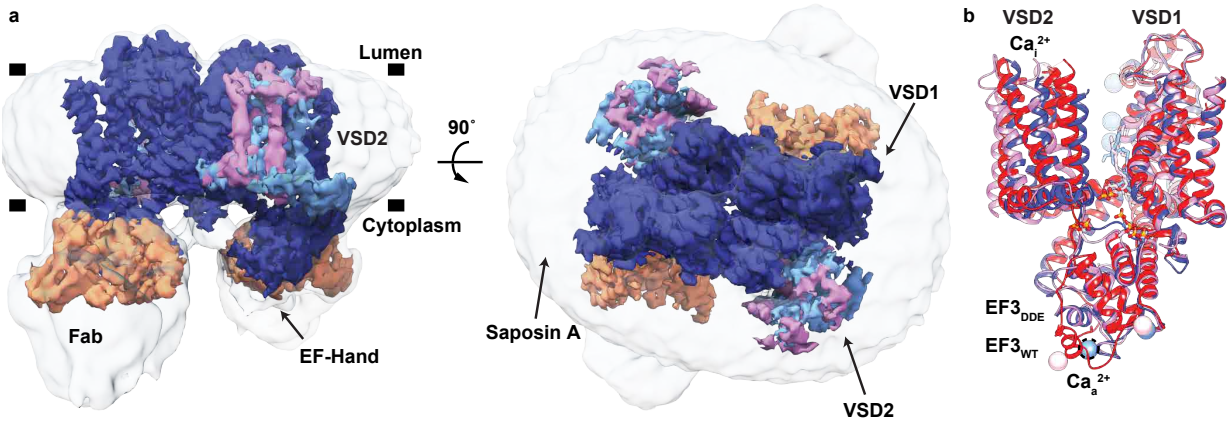

Figure 2.1: Cryo-EM Structure of the AtTPC1DDE–saposin A–Fab complex. (A) Side (Left) and top-down (Right) views of cryo-EM density. The composite map is colored to highlight high-resolution features of TPC1 (blue, EMDB entry no. 8957), VSD2 in state 1 (cyan, EMDB entry no. 8958) and state 2 (pink, EMDB entry no. 8960), and the Fab variable domains (orange, EMDB entry no. 8956). Unsharpened density is shown at low contour (transparent gray). Membrane boundaries (black bars) defined by the nanodisc are marked. (B) Overlay of AtTPC1WT (red, PDB ID code 5DQQ), state 1 (blue), and state 2 (pink). Cai2+ and Caa2+ denote sites of luminal inhibition and cytoplasmic activation by Ca2+ ions. Dash lines around Caa2+ indicate hypothetical position in cryo-EM structure. Ca2+ ions shown as colored balls.

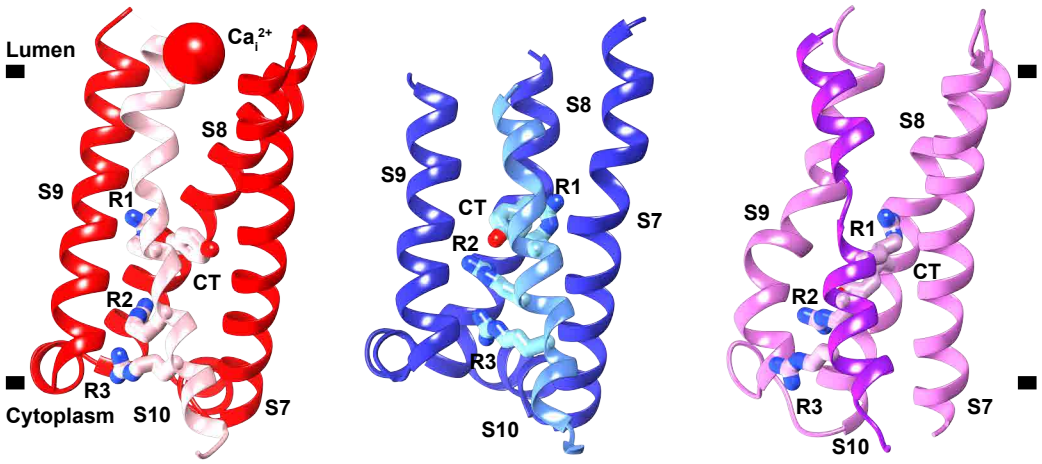

Figure 2.2: Three states of VSD2. View of VSD2 in the membrane plane from the center of the channel looking outward that illustrates the rotation and twisting of VSD2 helices S7, S8, S9, and S10. Connections to the pore domains are omitted for clarity. S10 is highlighted in each state with a different color than the other helices. Gating charges R1–R3 (R537, R540, and R543) and CT residue Y475 are shown. (Left) Resting-state AtTPC1WT (red, PDB ID code 5DQQ), (Center) AtTPC1DDE state 1 (blue), and (Right) AtTPC1DDE state 2 (pink).

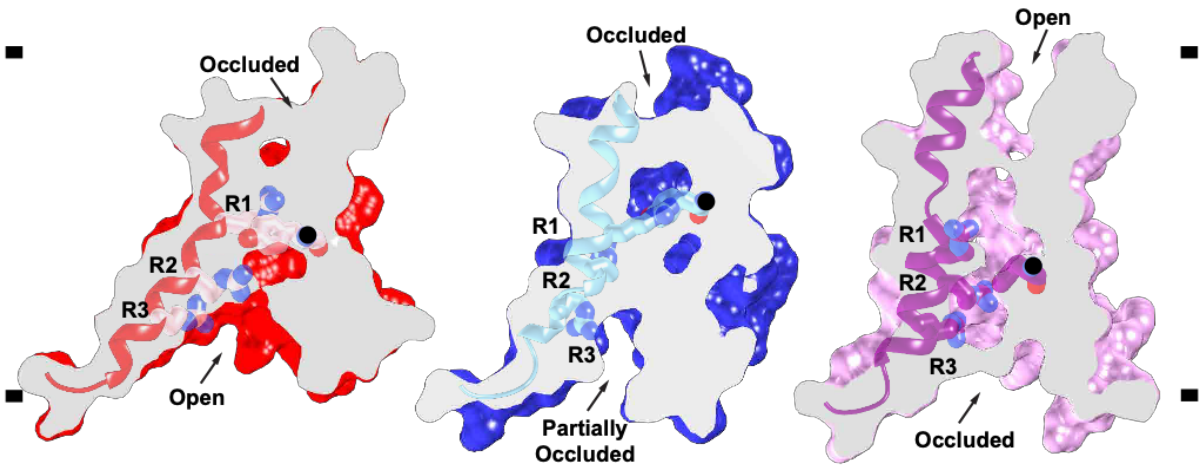

Figure 2.3: Activation of the voltage sensor. Side views of a common slice perpendicular to the membrane surface of VSD2 in AtTPC1WT resting state (red, PDB ID code 5DQQ) and AtTPC1DDE state 1 (blue) and state 2 (pink). S10 shown with gating charges R1–R3. The CT Cα position (black ball) is marked. Based on a structural alignment with respect to the pore helices S6–S7 of each structure.

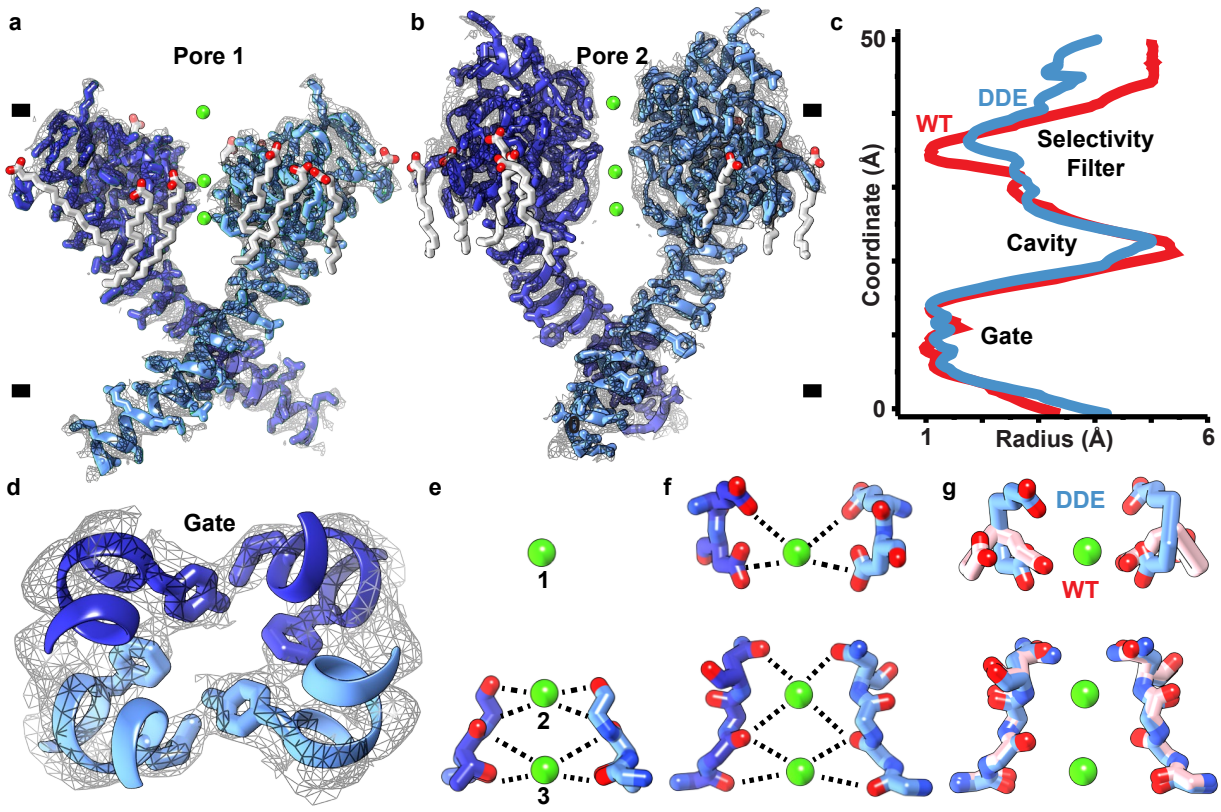

Figure 2.4: Ion permeation pathway. (A and B) Orthogonal side views through pore helices (A) S5–S6 (pore 1) and (B) S11–S12 (pore 2) of the channel homodimer overlaid with high-resolution cryo-EM density (gray mesh). (C) HOLE plot of pore radii along central channel coordinate of AtTPC1DDE (red) and AtTPC1WT (blue). (D) Top-down view through central pore. Gate residues Y305, L673, and F676 are shown. (E–G) Side views through the selectivity filter in (E) pore 1, (F) pore 2, and (G) an overlay of pore 2 of AtTPC1DDE (blue) and AtTPC1WT (pink). (Upper) E605 and D606 and (Lower) S265, T263, T264, V628, M629, and N631 selectivity filter residues are shown. Density for lipids (SI Appendix, Fig. S7) and ions is omitted for clarity.

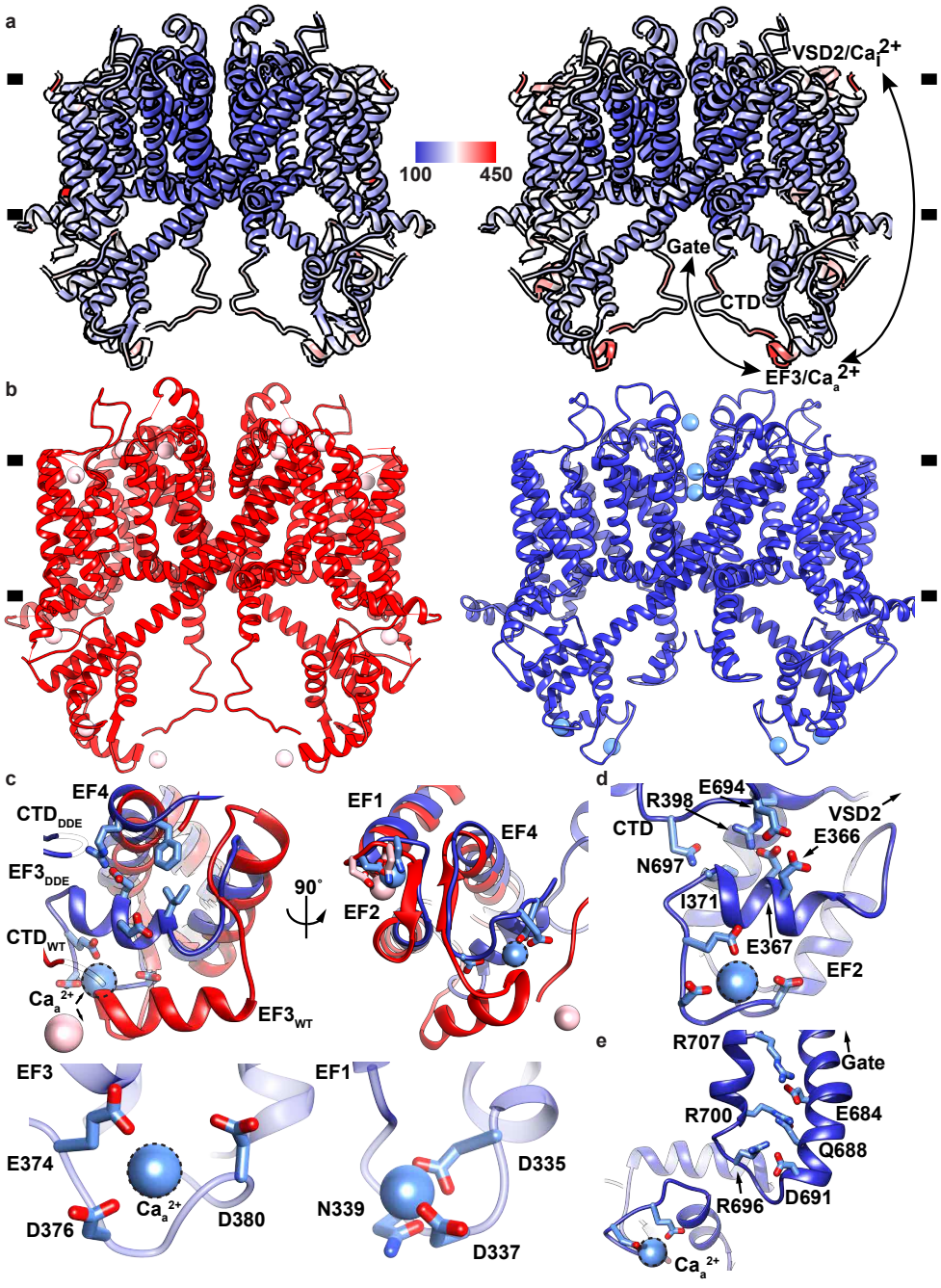

Figure 2.5: Dynamics of cytoplasmic domains. (A) Overlay of (Left) AtTPC1WT and (Right) AtTPC1DA crystal structures colored by B-factor value (100–450 Å2) (see Methods and SI Appendix, Supplementary Discussion). (B) Side views of AtTPC1WT (red) and AtTPC1DDE (blue). (C) Views from (Top Left) side and (Top Right) bottom of EF3 for overlaid AtTPC1DDE (blue) and AtTPC1WT crystal structures (red, PDB ID code 5DQQ). CTD interactions are omitted for clarity. Ca2+-ion binding sites in (Bottom Right) EF1–EF2 and (Bottom Left) EF3–EF4. (D) View of EF3-CTD and EF3-EF4 interactions and connection to VSD2. (E) Structure of the CTD in AtTPC1DDE and a possible coupling pathway to the pore gate and Caa2+. Dashed lines indicate the hypothetical Caa2+ ion position.

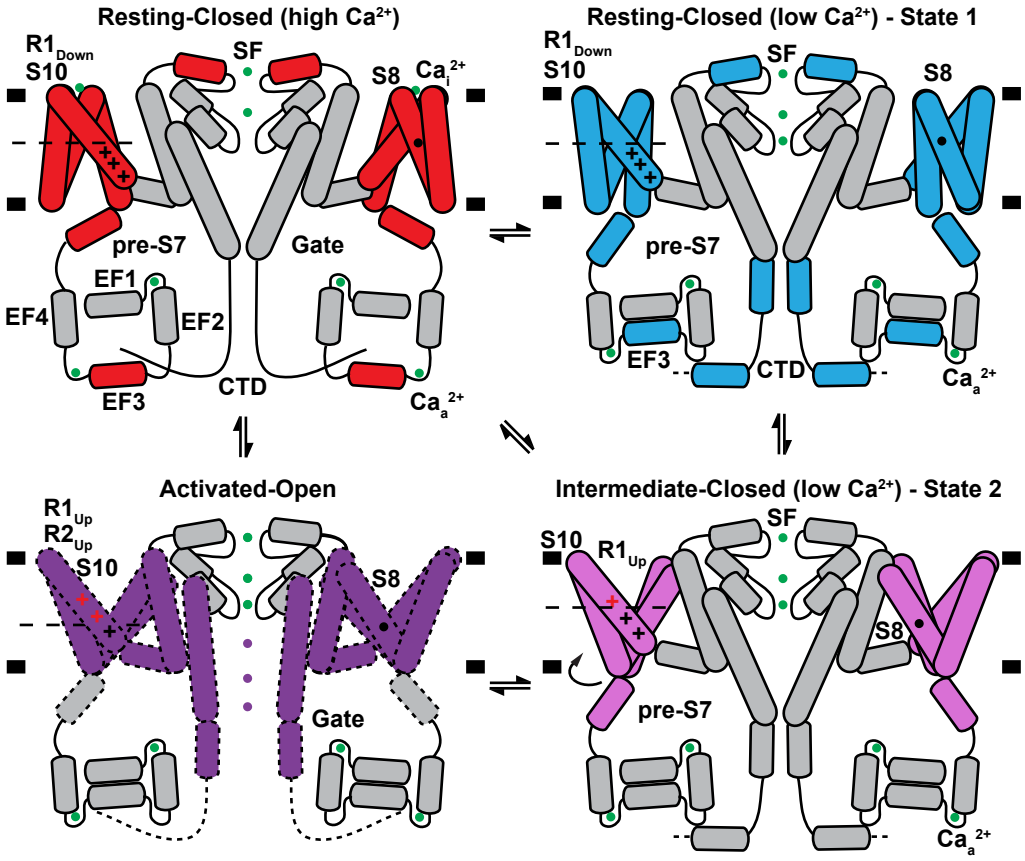

Figure 2.6: Mechanism of TPC1 channel activation. Schematic summarizing the conformations of VSD2, EF3, CTD, and selectivity filter (SF) observed in crystal and cryo-EM structures under high and low effective luminal Ca2+-ion concentrations. A potential model for coupling between luminal inhibition Cai2+, cytoplasmic activation Caa2+, voltage sensing, and channel gating is shown. Helices and ions that move between the AtTPC1WT resting state (red), AtTPC1DDE state 1 (cyan), AtTPC1DDE state 2 (pink), and hypothetical activated-open state (purple) are colored. Ca2+ ions are shown as green balls. Gating charges that change position with respect to the CT (dashed line) between states are colored red.

Table S1. Cryo-EM data collection and refinement statistics

Data collection[a]				
Voltage (kV)	300			
Pixel size (Å)	1.2156			
Defocus range (μm)	-0.8 – -2.0			
Total electron dose (e^-/A^2)	60			
Exposure time (s)	12			
Number of frames/image	60			
Number of images	3,408			
Image processing[a,b]				
Map	**High-res**	**State 1**	**State 2**	**Fab-bound**
Autopicked particles	996,035			
Particles post 2D	409,531			
Final particle number	224,577	44,353	67,308	224,577
Resolution (unmasked, Å)	3.7	4.2	4.3	4.0
Resolution (masked, Å)	3.3	3.7	3.7	3.7
Sharpening B-factor ($Å^2$)	-117	-95	-86	-104
Refinement[a,c]				
Number of atoms	8913	10682	10697	11641
R.m.s. deviations				
Bond lengths (Å)	0.017	0.014	0.009	0.018
Bond angles (°)	1.481	1.305	1.090	1.679
Ramachandran				
Favored (%)	91.49	91.59	92.95	88.32
Allowed (%)	8.41	8.25	6.89	11.39
Outlier (%)	0.10	0.16	0.16	0.29
Mean B-factor ($Å^2$)[d]	101.80	142.71	201.66	100.50
Molprobity Clashscore[e]	5.51	7.96	7.47	8.36
EMRinger score[f]	3.94	1.63	1.42	2.92
PDB ID[g]	6E1M	6E1N	6E1P	6E1K
EMDB ID[g]	8957	8958	8960	8956

[a] Data collection and processing detailed in Methods.
[b]Image processing schematic in Extended Data Fig. 4.
[c]Real-space refinement in PHENIX as outlined in Methods.
[d]As implemented in PHENIX, number of clashes per 1000 atoms.
[e]Calculated from real-space refinement in PHENIX.
[f]Calculated using EMRinger in PHENIX.
[g]Deposition codes for coordinates and maps deposited to the Protein Data Bank and Electron Microscopy Data Bank.

Table S2. X-ray Data Collection and Refinement Statistics for $AtTPC1_{DA}$

Data Collection	**$AtTPC1_{DA}$**[a]
Beamline	ALS 8.3.1 ALS 5.0.2 SSRL 12-2
Space Group	$C222_1$
Cell Dimensions	a=88.47, b=154.42, c=218.45, α=β=γ=90
Wavelength (Å)	1.000
Resolution[b]	30-3.5(4-3.5)
Number of reflections	19231
Completeness (%)	99.7(99.8)
Multiplicity	13.3(13.6)
I/σI	8(0.93)
$CC_{1/2}$[c]	100(57.7)
Rmeas (%)	23.6(362.2)
Anisotropy (a, b, c)[d]	3.5 x 6.0 x 4.5Å
Refinement	
Resolution (Å)	3.5 x 6.0 x 4.5Å[e]
No. reflections	8954
R_{work}/ R_{free}	0.3184/0.3519[f]
No. atoms	5092
Protein	5054
Ligand/ion	38
B-factor	114.26
R.M.S. deviations	
Bond lengths (Å)	0.003
Bond angles (°)	0.687
Ramachandran (%)	
Favored	93.09
Allowed	6.25
Outliers	0.66
PDB ID[g]	6CX0

[a]Uncorrected native data
[b]Values in parenthesis are for highest resolution shell.
[c]Percentage of correlation between intensities from random half-datasets, as calculated in XDS.
[d]Anisotropy as determined by Diffraction Anisotropy Server.
[e]Anisotropy-corrected data used for refinement with sharpening B-factor of -142.05 $Å^2$.
[f]5% of reflections were omitted from refinement for the calculation of R_{free}.
[g]Deposition codes for coordinates and maps deposited to the Protein Data Bank and Electron Microscopy Data Bank.

Methods

Protein Production

AtTPC1. X-ray and cryo-EM trials used AtTPC1 with deletion of residues 2-11(19). Antibody generation employed full-length AtTPC1. AtTPC1 constructs were expressed and purified by nickel affinity chromatography (NiNTA), thrombin cleavage, and size exclusion, as described previously(19). For reconstitution into saposin A lipoprotein nanoparticles and MSP nanodiscs, the size exclusion step was omitted after NiNTA, but performed after reconstitution. To introduce single cysteine labels for CW-EPR, a cysteine-less variant of AtTPC1, $AtTPC1_{cysless}$, was constructed to replace all native cysteines with serines (C93S, C101S, C159S, C347S, C392S, C574S, C577S, C580S, C687S, C728S). Cysteine substitutions for EPR spectroscopy were purified in the presence of 1mM TCEP during solubilization and binding to Nickel beads, but then removed during wash and elution steps to prevent interference with MTSL-labeling. $AtTPC1_{cysless}$ has identical biochemical behavior to wild-type AtTPC1.

Saposin A. Human saposin A (plasmid was a kind gift from J. Frauenfeld) was expressed and purified from *E. coli* Rosetta-gami 2(DE3) cells essentially as described(30). Several colonies from transformed cells were used to inoculate overnight 300 mL LB cultures containing 25 µg/mL chloramphenicol, 10 µg/mL tetracycline, and 15 µg/mL kanamycin at 37 ˚C. Overnight cultures were used to seed 6 L of Terrific Broth, grown to an absorbance value at 600 nm of 1. The temperature was adjusted to 20 ˚C 30 minutes prior to induction by 0.7 mM IPTG for 15 hours at 20 ˚C. Cells were harvested by centrifugation at 4,000x g for 10 minutes and resuspended in 200 mL 50 mM tris pH 7.4, 150 mM NaCl (Lysis Buffer) and frozen at -80 ˚C before further use. Bacterial pellets were lysed in the presence of 1 mM phenylmethylsulfonyl fluoride (PMSF) by sonication for 5 minutes, then clarified by centrifugation at 26,000x g for 20

minutes. The supernatant was then incubated at 70 ˚C for 10 minutes followed by centrifugation at 26,000x g for 20 minutes to remove contaminant proteins. Imidazole pH 7.4 was then added to 20 mM and passed through two HisTrap FF crude 5mL columns equilibrated in Lysis Buffer with 20 mM Imidazole pH 7.4 using a peristaltic pump. Following 50 mL washes with Lysis Buffer with 20 mM Imidazole pH 7.4 and Lysis Buffer with 35 mM Imidazole pH 7.4, pure human saposin A was eluted in 25 mL Lysis Buffer with 400 mM Imidazole pH 7.4 in 1.5 mL fractions. Fractions containing human saposin A were dialyzed against 1 L of Lysis Buffer with 4 mg of Tobacco Etch Virus (TEV) protease. The following morning an additional 2 mg of TEV was added with an exchange of the dialysis buffer and dialyzed at room temperature for 3 hours. Uncleaved saposin A and free TEV were removed by passing the protein through a single HisTrap FF crude 5 mL column equilibrated in Lysis Buffer with 20 mM Imidazole pH 7.4 and washed with 30 mL of Lysis Buffer with 20 mM Imidazole pH 7.4. The flow-through and wash fractions were pooled and concentrated in 5 kDa molecular weight cutoff concentrators and serially injected in 20 mg aliquots over TSKgel G3000SW 7 mm x 60 cm or Superdex S200 10/300 columns equilibrated in Lysis Buffer with 1 mM $CaCl_2$. High and low molecular weight peaks were observed during size exclusion. The low molecular weight, most consistent with the size of the saposin A monomers and dimers, was concentrated to 2 mg/mL for use in reconstitution of AtTPC1 and frozen at -80 ˚C. Final yields of human saposin A were 5-10 milligrams of human saposin A per liter of culture.

Membrane scaffold protein. Plasmid harboring His-tagged E3D1 variant of membrane scaffold protein (MSP) of the nanodiscs was obtained from Addgene (#20066). MSP was expressed, purified and cleaved with TEV protease as described(41) with minor modifications. Colonies of transformed BL21 (DE3) Gold cells (Stratagene) were used to inoculate overnight 30 mL LB

cultures containing 30 μg/mL kanamycin. Overnight cultures were used to inoculate 2 L of Terrific Broth, grown at 37 ˚C until OD_{600} of 1.3 and then induced with 1 mM IPTG for 3 hrs. Cultures were harvested by centrifugation at 4,000x g for 10 minutes, resuspended in 50 mM Tris pH 8.0, 300 mM NaCl (MSP Lysis Buffer) supplemented with 1% Triton X-100, protease inhibitor tablet and 1 mM PMSF. Microtip sonicator (Branson) was used to lyse the cells for 3 cycles at 1s on, 1 off and at 60% amplitude for 3 minutes each. For each 1L culture 1 mL of NiNTA resin equilibrated with MSP Lysis Buffer was used in batch-binding for 1 hour at 4 ˚C. Resin was then washed with MSP Lysis Buffer supplemented with: 1) 1% Triton X-100 - 10 column volumes (CVs), 2) 50 mM sodium cholate, 20 mM imidazole – 5 CVs, 3) 50 mM imidazole – 7 CVs. MSP was eluted with 4 CVs of MSP Lysis Buffer supplemented with 400 mM imidazole. TEV cleavage was performed overnight in dialysis against 4 L of 50 mM Hepes pH 7.5 and 200 mM NaCl. Uncut protein was removed with subtractive step on NiNTA resin and cleaved MSP was concentrated to 5 mg/mL using Millipore concentrators with 10 kDa molecular weight cutoff and frozen in aliquots at -80 ˚C. Typical yield of MSP E3D1 from 1 L culture was 15 mg.

Antibodies. Monoclonal antibodies were expressed and purified from hybridoma culture supernatants using standard methods in the Monoclonal Antibody Core Facility at OHSU (Dan Cawley). 4B8 Fab fragment was generated by papain digestion 1/20 Papain:4B8 (w/w) at 30 ˚C for 1 hour in the presence of 5 mM L-cysteine and quenched with 20 mM iodoacetamide. Full-length IgG and Fc regions were removed via protein A chromatography and the flow-through containing 4B8 Fab was concentrated and purified by TSK3000/Superdex200 size exclusion chromatography in 20 mM Hepes pH 7.4, 0.2M NaCl, 5% Glycerol.

Antibody fragments (Fabs) generated by phage display were expressed and purified essentially as described(42) from constructs subcloned into the expression vectors pRH2.2 or

pSFV4 (gift from S. Sidhu). DNA was transformed into BL21-Gold(DE3) (Agilent) and used directly to set up 15 mL overnight starter cultures in 2xYT media supplemented with 50 ug/mL ampicillin. Cultures were then inoculated into 1 L of 2xYT media, grown until OD_{600} of ~0.8-1.0, induced with 1 mM IPTG for 4 hours at 37 °C. Cells were harvested by centrifugation and disrupted in lysis buffer containing 20 mM sodium phosphate dibasic pH 7.4, 500 mM NaCl, 1 mM PMSF, and 2 mM DNase, using sonicator (Branson). Lysate was heated to 55 °C for 30 minutes, cleared by centrifugation and incubated with 1 mL of MabSelect ProteinA resin (GE Healthcare) in batch for 1 hour at 4 °C. Resin was washed with 15 column volumes of 20 mM sodium phosphate dibasic pH 7.4, 500 mM NaCl and then eluted with 10 ml 0.1 M acetic acid into tubes containing 1 mL of 1 M Hepes pH 7.5 to immediately neutralize elutions containing Fab fragments. Fabs were then dialyzed against 4 L of 50 mM HEPES pH 7.5 and 200 mM NaCl, concentrated with Millipore concentrators with 30 kDa molecular weight cutoff and stored in aliquots at -80 ˚C. Typical yield from 1 L culture varied depending on Fab fragment and was between 0.5 – 3 mg. For cryo-EM studies Fab CAT06 was modified with H12 elbow variant as described previously(43), resulting in the CAT06/H12 antibody fragment. Briefly, the H12 elbow variant exchanges heavy chain residues (112)SSASTK(117) (numbering according to Kabat (44)) to (112)FNQI-K(117) with one position deleted from the sequence.

Saposin A and Nanodisc Reconstitution

Lipids. All lipids were prepared from thin films. Lipids were dissolved in chloroform, aliquoted into glass vials, dried under nitrogen, and stored at -20 ˚C dry. Unless otherwise noted, resuspending lipids was accomplished by adding buffer with or without detergent and sonicating 10-30 minutes until clear.

Saposin A nanoparticles. Saposin A nanoparticles containing AtTPC1 were formed by mixing AtTPC1 alone or AtTPC1-Cat06/H12 Fab complexes with soy polar lipids and saposin A in a 1:8:5-10 ratio by mass. A typical preparation consisted of 2.4 mg (8 mg/mL) of NiNTA purified AtTPC1 incubated with 2.4 mg (9 mg/mL) of protein A purified CAT06/H12 (adjusted to 0.05% DDM, 1 mM $CaCl_2$), incubated at room temperature for 5-10 minutes. AtTPC1-Cat06/H12 Fab complexes were then mixed with 4.8 mL of 5 mg/mL soy polar lipids (diluted from a 25 mg/mL stock in 1% DDM) dissolved in Size Exclusion Buffer (20 mM Hepes pH 7.3, 0.2 M NaCl, 5% Glycerol, 1 mM $CaCl_2$, 0.05% DDM) and incubated at room temperature for 30 minutes. Then 9.6 mL (2 mg/mL) saposin A was added, incubated 1 hour at room temperature, then diluted to 40 mL with Size Exclusion Buffer. Detergent was removed by adding 1 g of activated, washed, Bio-Beads SM2 (BIO-RAD) resin overnight at 4˚C. Bio-Beads were activated by incubation in methanol and successively washed with copious amounts of water. The following morning, beads were removed by filtration through 5 µm syringe filter. 0.5 molar equivalent of Fab CAT06/H12 was added, incubated 30 minutes at 4 ˚C, then concentrated to ~0.3 mL in a 100 kDa MWCO concentrator, and filtered prior to injection on a TSK4000 or Superose 6 column equilibrated in Nanodisc Size Exclusion Buffer (20 mM Hepes pH 7.3, 0.2 M NaCl, 1 mM $CaCl_2$). A single fraction was selected for cryo-EM analysis by screening for homogeneous particles by negative-stain EM (SI Appendix, Fig. S6b-d). Cryo-EM grids were frozen following ultracentrifugation at 100,000x g (TLA-55) for 5 minutes at 4 ˚C without further concentration. AtTPC1-CAT06/H12-saposin A complexes typically eluted from size exclusion at 0.5-1 mg/mL. 16 lipids are observed bound to $AtTPC1_{DDE}$ (SI Appendix, Fig. S7).

MSP nanodiscs. Reconstitution of AtTPC1 into E3D1 nanodiscs was performed using standard protocols(45). For the purpose of antibody generation by phage display, full-length $AtTPC1_{WT}$

was reconstituted into nanodiscs using biotinylated version of MSP E3D1, and size exclusion fractions corresponding to AtTPC1 in biotinylated nanodiscs were used without the removal of empty nanodiscs. Final mixed lipid-detergent micelles used in reconstitution contained 10 mM soy polar extract, 1 mM CHS, and 30 mM DDM. Nanodisc assembly mix was prepared using purified TPC1, mixed micelles and MSP at 2:10:1000 ratio. All components were mixed together in Nanodisc Size Exclusion Buffer and incubated on ice for 1 hour. Next, 400-500 mg activated Bio-Beads were added per each ml of assembly mix, and the reconstitution reaction was left shaking overnight at 4°C. As a control, empty nanodiscs were prepared using the same phospholipids. All nanodisc samples for phage display experiments were concentrated, supplemented with 5% w/v sucrose, aliquoted, flash-frozen in liquid nitrogen, and kept at -80°C.

Proteoliposomes. Proteoliposomes of full-length wild-type AtTPC1 were formed by resuspending 20mg of soy polar lipids dried from chloroform resuspended in 4 mL Nanodisc Size Exclusion Buffer, subjected to 10x alternating liquid Nitrogen and warm water bath freeze-thaw cycles, then sonicated for 10 min. The opaque mixture was then passed through an Avestin hand extruder with a 400 nm pore size 10x until mildly translucent. Vesicles were disrupted by addition of 69.8 µL 10% DDM added (4 mM final), 12.1 µL 2% CHS in 10% DDM added (0.1 mM final), and 1 mM $CaCl_2$, and stirred 30 minutes at room temperature. 2 mg of AtTPC1 was added to disrupted liposomes (1:10 protein:lipid ratio) and stirred for 1 hour at room temperature using a magnetic “flea” stir bar. To form proteoliposomes, methanol washed Bio-Beads were added in increments of 300 mg, 300 mg, 500 mg, and 1 g in 1-hour intervals at room temperature. The last incubation was done at 4 ˚C overnight. The following morning the samples were centrifuged at 100,000x g for 1 hour in a table-top ultracentrifuge (TLA-55). The proteoliposome pellet was resuspended in in 0.4 mL of Nanodisc Size Exclusion Buffer. The

concentration was estimated by gel and frozen in liquid Nitrogen and stored at -80 ˚C. Empty liposomes were made in a similar fashion by substituting AtTPC1 protein with Size Exclusion Buffer.

Antibody Generation

Hybridoma. Hybridoma cell lines were generated by standard methods at OHSU by Daniel Cawley. Briefly, four Balb/c mice were injected with 25 µg of AtTPC1 proteoliposomes at 0 and 14 days. On day 26, serum was prepared and tested for antibody titer in ELISA. The mice with the highest titers were used to derive hybridomas. The two best responding mice were injected on day 45-55 with 10 µg Ag as a final boost. 4 days later, spleen cells are fused with P3X mouse myeloma cells. Hybridomas were assayed 12 days later in ELISA. All candidate cell lines were expanded and given a secondary ELISA screen 12-14 days later. All antigen specific antibodies were made available as culture supernates for screening. All candidate cell lines are frozen in liquid nitrogen. 14 hybridoma antibodies were identified that specifically bind to immobilized biotinylated AtTPC1 in DDM detergent by ELISA. To select for antibodies that recognize 3D structural epitopes a counter-selection against antibodies that bind linear epitopes on denatured protein in 8M Urea was performed, yielding 5 antibodies that bind only under native conditions by ELISA. Selection of high-affinity antibodies that were capable of complex formation was conducted by fluorescence size exclusion chromatography(46) (FSEC) using FITC-labeled AtTPC1 and hybridoma supernatants containing 10-50 µg/mL whole IgG. FSEC samples were prepared by mixing 1µg FITC-Labeled AtTPC1 with 0.4 mL hybridoma supernatants (supplemented with components to make Size exclusion buffer +0.03 mg/mL Soy Polar Lipids) in a total volume of 490 µL of Size exclusion buffer. Samples were incubated at 25 ˚C for 1 hour or 4 ˚C for 4-5 hours and injected on a Superose 6 column, 0.4 mL/min, equilibrated in Size

exclusion buffer at 4 ˚C, using an autosampler and inline fluorescence detector set at excitation=495 nm and emission=518 nm. The fluorescence detector (Shimadzu RF-10AXL) was calibrated before use by injecting varying amounts of FITC-AtTPC1 (0.1 ng-1 µg) with known labelling efficiency.

Phage Display. To generate Fabs, the efficiency of biotinylation of $AtTPC1_{WT}$-E3D1 nanodiscs was evaluated by pull-down on streptavidin-coated magnetic beads (Promega). Library sorting steps were performed using Fab Library E (DNA kindly provided by S. Koide(47)) based on previous protocols(31, 48). Six independent phage library sorting experiments were performed against biotinylated $AtTPC1_{WT}$ -E3D1 nanodiscs in 2 buffers containing 20 mM Hepes pH 7.3, 200 mM NaCl, 5% glycerol, 1% BSA, and either 1 mM $CaCl_2$ or 1 mM EGTA. Additionally, for each $CaCl_2$ or EGTA condition, sorting was carried out in the presence of following ligands: either 1 µM NAADP, 1 µM trans-NED19, or no ligand control to maximize the number of multiple states of TPC1 channel during sorting (Sorting Buffer). Total of five rounds of phage library sorting were performed for each sample with decreasing concentration of immobilized biotinylated TPC1-E3D1 nanodiscs between subsequent rounds in following order 1000 nM, 600 nM, 200 nM, 200 nM and 100 nM. Round 1 of sorting was performed manually using nanodisc bound to streptavidin-coated magnetic beads, and upon washing with respective Sorting Buffer, whole beads were used to infect log phase *E. coli* XL-1 strain (Stratagene) in the 2xYT media (Fisher) supplemented with 50 µg/ml ampicillin and 10^9 pfu/ml of KO7 helper phage (NEB) overnight at 37 °C and 280 rpm to amplify the phage particles. The amplified phage particles after round 1 were used as an input for four additional rounds of library sorting performed semi-automatically with a KingFisher magnetic bead handler (Thermo) according to described protocols(49). Starting from round 2, in every step except elution, the buffer was supplemented

with 10-fold molar excess of non-biotinylated empty E3D1 nanodiscs to counter-select for MSP-, lipid-, and non-specific phage particles. Finally, in each of rounds 2-5, phage particles were eluted from magnetic beads by 15-minutes incubation with 1% Fos-Choline-12 in respective Sorting Buffer.

Initial validation of selection clones was performed by single point direct phage ELISA using clones from round 3, 4 and 5. Amplified phage particles at 10-fold dilution were assayed against 50 nM biotinylated nanodiscs (either empty or with AtTPC1) using HRP-conjugated anti-M13 monoclonal antibody (GE Healthcare, #27-9421-01). Assays were performed in respective Sorting Buffer supplemented with 2% BSA. Each Fab clone with A_{450} signal above 0.2 (four times the average background level of the assay) was sequenced; unique Fabs were sub-cloned into pSVF4 or pRH2.2 vectors (kind gift of S. Sidhu), and purified as described above. In total 16 unique Fab sequences were obtained from total of 192 single colonies screened; 9 Fabs from library sorting with $CaCl_2$ and 7 Fabs from library sorting with EGTA.

Cryo-EM Structure Determination

Sample Preparation. Samples were analyzed by negative-stain EM to determine suitability for cryo-EM. To prepare grids, 3 μl of sample at 10–50 μg ml^{-1} was applied to a glow discharged continuous carbon grid, which was then treated with 0.75% (w/v) uranyl formate. Grids were imaged on an FEI Tecnai T12 microscope operated at 120kV at a nominal magnification of 52,000× using an UltraScan 4000 camera (Gatan) or an FEI Tecnai T20 microscope operated at 200kV and at a nominal magnification of 80,000× using a TemCam-F816 8k × 8k CMOS camera (TVIPS) camera, corresponding to pixel sizes of 2.21 Å and 0.95 Å, respectively, on the specimen.

Grids for cryo-EM were prepared with FEI Mark IV vitrobot. Quantafoil R1.2/1.3 400 mesh holey carbon grids (EMS) were glow-discharged for 30 s. Then 2.5 µl protein sample at a concentration of 0.6-1.5 mg ml^{-1} was applied onto the carbon face of the grids. The grids were blotted with Whatman#1 filter paper for 2-4 s at 100% humidity and plunge frozen in liquid ethane. The grids were loaded onto a 300kV Polara (FEI) with a K2 Summit direct electron detector (Gatan). Data were collected at nominal magnification of 31,000×, corresponding to a physical pixel size of 1.2156 Å (0.6078 Å super resolution pixel size) on the specimen with a dose rate of 7.6 electrons per physical pixel per second. Images were recorded with SerialEM in super-resolution counting mode and a defocus range of −0.8 to −2.0 µm. A total exposure of 12 s was used, with 0.2 s subframes (60 total frames) to give a total dose of 60 electrons per $Å^2$ (1.35 electrons per $Å^2$ per subframe). Data for $AtTPC1_{WT}$ in saposin A was also collected at the Janelia Cryo-EM facility FEI Titan Krios microscope operated at 300kV with a K2 camera with a physical pixel size of 1.02 Å.

Image Processing. For negative-stain data, GCTF(50), Gautomatch (Kai Zhang, url: https://www.mrc-lmb.cam.ac.uk/kzhang/), and RELION-2(51) were used for CTF estimation, particle picking, and 2D classification, respectively. For cryo-EM data, dose-fractionated super-resolution image stacks were drift corrected and binned 2×2 by Fourier cropping using MotionCor2(52) (after discarding the first frame). CTF determination and particle picking was performed on motion-corrected sums without dose-weighting using GCTF and Gautomatch. To generate particle picking templates and initial models a Gaussian reference was used to pick particles and 2D classification was performed in RELION-2 followed by *ab-initio* reconstruction in cryoSPARC. Particles were then picked using six 2D classes as templates. 2D classification, 3D classification and refinement procedures were carried out using and RELION-2 and

cryoSPARC(53) (SI Appendix, Fig. S3). After 3D classification the reconstruction was filtered to 30 Å resolution and used as an initial reference model for 3D refinement in cryoSPARC v2 using the beta version of non-uniform refinement yielding a reconstruction with a gold-standard Fourier shell correlation of 3.5 Å with a 0.143 cutoff criterion. The map from cryoSPARC was used for modeling the Fab variable domain. The final 3.3 Å high-resolution reconstruction was performed in RELION-2 using 3D auto-refinement by masking out the saposin A membrane belt and the Fab using a mask created from a 30 Å low-pass filtered model of $AtTPC1_{WT}$. Local resolution estimates were performed using RELION-2. The final maps were sharpened in RELION-2 using a B-factor of -104 and -117 $Å^2$ for the TPC1-Fab-saposin and TPC1-only reconstructions, respectively.

State 1 and 2 were identified by focused classification of VSD2 without image alignment using the angles determined from the high-resolution reconstruction (SI Appendix, Fig. S3). Focused classification benefitted from applying C2 symmetry. After 3D classification each particle set was refined in RELION-2 with global angular searches using a 30Å low pass filtered reconstruction of the combined dataset. The maps for state 1 and 2 extend to 3.7 Å as determined by the gold-standard FSC. These maps were used to build atomic models for VSD2 with local resolution in this region ranging from 4-6 Å as estimated by RELION-2 (Table S1). The final maps were sharpened in RELION-2 using a B-factor of -95 and -86 $Å^2$ for the state and state 2 reconstructions, respectively.

Structure Determination and Refinement. The entire structure of $AtTPC1_{DDE}$ excluding VSD2 was built into the highest resolution map (High-res; Table S1) manually after initial real-space flexible fitting and refinement of the $AtTPC1_{WT}$ structure into the map using Rosetta (54) with the electron scattering table. Manual fitting in COOT(55), followed by real-space coordinate and

B-factor/atomic displacement factor refinement in PHENIX(56) were used in *de novo* building of the NTD, EF-hand, CTD, Ca^{2+}-ions, lipid molecules (palmitic acid and phosphatidic acid), and the Fab-AtTPC1$_{DDE}$ interface. This map was calculated with a mask around TPC1, excluding the Fab. A structure of the Fab-complex (Fab-bound; Table S1) was determined from the same dataset by extending the mask to include the Fab variable domains (V_H and V_L). The Fab was built using a homologous structure of a Fab from the same library (PDB 3PGF) with the variable CDR loops deleted.

Building of the state 1 (State 1; Table S1)was accomplished by rigid body alignment of the AtTPC1$_{WT}$ structure to the cryo-EM map using CHIMERA (57) followed by flexible fitting and refinement in Rosetta, and extensive manual fitting in COOT. State 2 (State 2; Table S1) was built by first rotating VSD2 of AtTPC1$_{WT}$ to place S10. Movement of S7-S9 around the S10 axis was done manually in real-space. Gating charges R1-R3 were placed in favored rotamer positions using the rotamer library in COOT and PHENIX, while applying the additional restraint that R1-R3 must contact solvent, a polar side chain, or counter charge in the membrane. One position satisfied these criteria for each gating charge.

Model validation employed MolProbity(58) and EMRinger(59). Low resolution maps of AtTPC1$_{WT}$-4B8 were interpreted by flexible fitting of the AtTPC1$_{WT}$ crystal structure and a homology model of 4B8 in real-space using Rosetta.

Crystal Structure Determination. AtTPC1 D376A (AtTPC1$_{DA}$) crystals were obtained in the presence of $CaCl_2$, CHS, soy polar lipids, and 1mM trans-NED19 (NED19), using HiLiDe(60) as described previously(19). Average diffraction was 4 Å, with 10% diffracting to 3.5-3.7 Å resolution, the best being 3.5 Å. Anisotropic resolution was determined using the CCP4 program Truncate(61) and the UCLA Anisotropy Server(62). Crystals were partially dehydrated by

incubation with additional 15% (v/v) of polyethylene glycol 300 prior to freezing in liquid nitrogen.

X-ray diffraction datasets were collected at the Advanced Light Source (ALS) Beamlines 8.3.1 and 5.0.2 and at Stanford Synchrotron Radiation Lightsource (SSRL) Beamline 12-2. Data were reduced using XDS(63). The best native dataset extends to overall resolution 3.5 x 6.0 x 4.5 Å (ref.(62)). Phases were calculated by molecular replacement using PHASER(64) and AtTPC1 wild-type (PDBID 5DQQ) as a search model. Structure interpretation was using COOT(55), with refinement in PHENIX(56). The structure of $AtTPC1_{DA}$ was refined to 3.5 Å resolution with final R_{work}/R_{free} of 31.84 % and 35.19%. A sharpening B-factor of -142.05 $Å^2$ was used for refinement, as described previously(19). Analysis by Molprobity shows Ramachandran geometries of 93.09%, 6.25%, and 0.66% for favored, allowed, and outliers. The structure contains 11.31% rotamer outliers. For comparison of B-factors between $AtTPC1_{WT}$ (mean Wilson B-factor 108 $Å^2$; PDB ID 5DQQ)(19) and $AtTPC1_{DA}$ (mean Wilson B-factor 109.86 $Å^2$) structures, B-factors were first scaled by adding the difference in mean wilson B-factor (1.86 $Å^2$) to the mean wilson B-factor of the wild-type AtTPC1 crystal structure (PDBID 5DQQ)(19).

Sample Preparation for CW-EPR. Concentrated (7-12 mg/mL) NiNTA-purified $AtTPC1_{cysless}$ mutations were incubated with 10-fold molar excess MTSL (MTSL; Toronto Research Chemicals, Inc) dissolved at 10 mg/mL in DMSO for 2 hours at room temperature. The samples were then split in half and treated with either 1mM $CaCl_2$ or 5mM EGTA pH 7.4 prior to filtration and purification by size exclusion chromatography in 1mM $CaCl_2$ or 5mM EGTA pH 7.4, respectively. $AtTPC1_{cysless}$ has identical biochemical behavior to $AtTPC1_{WT}$ and maintains structural integrity as evidenced by negative-stain EM analysis. Fractions containing labeled $AtTPC1_{cysless}$ were pooled and concentrated to 5 mg/mL for EPR measurements.

EPR Data Collection. For continuous wave (CW) EPR experiments, X-band spectra were collected on a Varian E-102 Century series spectrometer fitted with a loop-gap resonator (Medical Advances, Milwaukee, WI). Samples (10 uL) were contained in a 0.64/0.80 mm (i.d./o.d.) quartz capillary (Vitrocom, Mountain Lakes, NJ) and spectra were recorded at room temperature over 100 G with an incident microwave power of 2 mW, modulation amplitude of 1 G, and modulation frequency of 100 kHz; typical total scan times were 5 minutes. CW spectra were normalized and corrected for minute deviations in baseline prior to comparison and analysis. All data were plotted using Origin 6 after normalizing the area under integrated CW spectrum.

Cryo-EM structural data of $AtTPC1_{DDE}$ has been deposited to the Protein Data Bank under accession codes 6E1K, 6E1M, 6E1N, 6E1P and the Electron Microscopy Data Bank under accession codes 8956, 8957, 8958, 8960. X-ray structural data of $AtTPC1_{DA}$ has been deposited to the Protein Data Bank under accession code 6CX0. Correspondence and requests for materials should be addressed to R.M.S (stroud@msg.ucsf.edu) and Y.C. (ycheng@ucsf.edu).

References

1. B. Hille, *Ion Channels of Excitable Membranes, Third Edition*, 3rd Edition edition (Sinauer Associates, 2001).

2. X. Tao, A. Lee, W. Limapichat, D. A. Dougherty, R. MacKinnon, A Gating Charge Transfer Center in Voltage Sensors. *Science* **328**, 67–73 (2010).

3. S. K. Aggarwal, R. MacKinnon, Contribution of the S4 Segment to Gating Charge in the Shaker K+ Channel. *Neuron* **16**, 1169–1177 (1996).

4. S.-A. Seoh, D. Sigg, D. M. Papazian, F. Bezanilla, Voltage-Sensing Residues in the S2 and S4 Segments of the Shaker K+ Channel. *Neuron* **16**, 1159–1167 (1996).

5. W. A. Catterall, Molecular Properties of Voltage-Sensitive Sodium Channels. *Annu. Rev. Biochem.* **55**, 953–985 (1986).

6. H. R. Guy, P. Seetharamulu, Molecular model of the action potential sodium channel. *Proc. Natl. Acad. Sci. U. S. A.* **83**, 508–512 (1986).

7. C. S. Gandhi, E. Y. Isacoff, Molecular Models of Voltage Sensing. *J. Gen. Physiol.* **120**, 455–463 (2002).

8. Y. Jiang, V. Ruta, J. Chen, A. Lee, R. MacKinnon, The principle of gating charge movement in a voltage-dependent K+ channel. *Nature* **423**, 42–48 (2003).

9. F. Bezanilla, The Voltage Sensor in Voltage-Dependent Ion Channels. *Physiol. Rev.* **80**, 555–592 (2000).

10. F. Bezanilla, E. Perozo, E. Stefani, Gating of Shaker K+ channels: II. The components of gating currents and a model of channel activation. *Biophys. J.* **66**, 1011–1021 (1994).

11. Z. Lu, A. M. Klem, Y. Ramu, Coupling between Voltage Sensors and Activation Gate in Voltage-gated K+ Channels. *J. Gen. Physiol.* **120**, 663–676 (2002).

12. E. Perozo, D. M. Cortes, L. G. Cuello, Three-dimensional architecture and gating mechanism of a K+ channel studied by EPR spectroscopy. *Nat. Struct. Mol. Biol.* **5**, 459–469 (1998).

13. J. Payandeh, T. Scheuer, N. Zheng, W. A. Catterall, The crystal structure of a voltage-gated sodium channel. *Nature* **475**, 353–358 (2011).

14. Q. Li, *et al.*, Structural mechanism of voltage-dependent gating in an isolated voltage-sensing domain. *Nat. Struct. Mol. Biol.* **21**, 244–252 (2014).

15. X. Zhang, *et al.*, Crystal structure of an orthologue of the NaChBac voltage-gated sodium channel. *Nature* **486**, 130–134 (2012).

16. S. B. Long, E. B. Campbell, R. Mackinnon, Crystal structure of a mammalian voltage-dependent Shaker family K+ channel. *Science* **309**, 897–903 (2005).

17. V. Yarov-Yarovoy, D. Baker, W. A. Catterall, Voltage sensor conformations in the open and closed states in rosetta structural models of K+ channels. *Proc. Natl. Acad. Sci.* **103**, 7292–7297 (2006).

18. V. Yarov-Yarovoy, *et al.*, Structural basis for gating charge movement in the voltage sensor of a sodium channel. *Proc. Natl. Acad. Sci.* **109**, E93–E102 (2012).

19. A. F. Kintzer, R. M. Stroud, Structure, inhibition and regulation of two-pore channel TPC1 from Arabidopsis thaliana. *Nature* **531**, 258–264 (2016).

20. J. Guo, *et al.*, Structure of the voltage-gated two-pore channel TPC1 from Arabidopsis thaliana. *Nature* **531**, 196–201 (2016).

21. A. F. Kintzer, R. M. Stroud, On the structure and mechanism of two-pore channels. *FEBS J.* **285**, 233–243 (2018).

22. R. Hedrich, I. Marten, TPC1 – SV Channels Gain Shape. *Mol. Plant* **4**, 428–441 (2011).

23. S. Patel, Function and dysfunction of two-pore channels. *Sci Signal* **8**, re7–re7 (2015).

24. X. Wang, *et al.*, TPC proteins are phosphoinositide- activated sodium-selective ion channels in endosomes and lysosomes. *Cell* **151**, 372–383 (2012).

25. Y. Sakurai, *et al.*, Two-pore channels control Ebola virus host cell entry and are drug targets for disease treatment. *Science* **347**, 995–998 (2015).

26. C. Cang, B. Bekele, D. Ren, The voltage-gated sodium channel TPC1 confers endolysosomal excitability. *Nat. Chem. Biol.* **10**, 463–469 (2014).

27. R. Hedrich, E. Neher, Cytoplasmic calcium regulates voltage-dependent ion channels in plant vacuoles. *Nature* **329**, 833–836 (1987).

28. D. Beyhl, *et al.*, The fou2 mutation in the major vacuolar cation channel TPC1 confers tolerance to inhibitory luminal calcium. *Plant J.* **58**, 715–723 (2009).

29. C. Schulze, H. Sticht, P. Meyerhoff, P. Dietrich, Differential contribution of EF-hands to the Ca2+-dependent activation in the plant two-pore channel TPC1. *Plant J.* **68**, 424–432 (2011).

30. J. Frauenfeld, *et al.*, A saposin-lipoprotein nanoparticle system for membrane proteins. *Nat. Methods* **13**, 345–351 (2016).

31. P. K. Dominik, *et al.*, Conformational Chaperones for Structural Studies of Membrane Proteins Using Antibody Phage Display with Nanodiscs. *Structure* **24**, 300–309 (2016).

32. S. Wu, *et al.*, Fabs enable single particle cryoEM studies of small proteins. *Struct. Lond. Engl. 1993* **20**, 582–592 (2012).

33. J. Guo, W. Zeng, Y. Jiang, Tuning the ion selectivity of two-pore channels. *Proc. Natl. Acad. Sci.* **114**, 1009–1014 (2017).

34. W. A. Catterall, G. Wisedchaisri, N. Zheng, The Chemical Basis for Electrical Signaling. *Nat. Chem. Biol.* **13**, 455–463 (2017).

35. J. She, *et al.*, Structural insights into the voltage and phospholipid activation of the mammalian TPC1 channel. *Nature* **556**, 130–134 (2018).

36. L. Tang, *et al.*, Structural basis for inhibition of a voltage-gated Ca2+ channel by Ca2+ antagonist drugs. *Nature* **537**, 117–121 (2016).

37. L. Zhang, *et al.*, Ionic liquid-based ultrasound-assisted extraction of fangchinoline and tetrandrine from Stephaniae tetrandrae. *J. Sep. Sci.* **32**, 3550–3554 (2009).

38. P. V. K. Gutla, A. Boccaccio, A. De Angeli, F. Gambale, A. Carpaneto, Modulation of plant TPC channels by polyunsaturated fatty acids. *J. Exp. Bot.* **63**, 6187–6197 (2012).

39. E. Cao, M. Liao, Y. Cheng, D. Julius, TRPV1 structures in distinct conformations reveal activation mechanisms. *Nature* **504**, 113–118 (2013).

40. N. Larisch, *et al.*, The function of the two-pore channel TPC1 depends on dimerization of its carboxy-terminal helix. *Cell. Mol. Life Sci.* **73**, 2565–2581 (2016).

41. F. J. D. Alvarez, C. Orelle, A. L. Davidson, Functional Reconstitution of an ABC Transporter in Nanodiscs for Use in Electron Paramagnetic Resonance Spectroscopy. *J. Am. Chem. Soc.* **132**, 9513–9515 (2010).

42. M. T. Borowska, P. K. Dominik, S. A. Anghel, A. A. Kossiakoff, R. J. Keenan, A YidC-like Protein in the Archaeal Plasma Membrane. *Struct. Lond. Engl. 1993* **23**, 1715–1724 (2015).

43. L. J. Bailey, *et al.*, Locking the Elbow: Improved Antibody Fab Fragments as Chaperones for Structure Determination. *J. Mol. Biol.* (2017) https:/doi.org/10.1016/j.jmb.2017.12.012.

44. E. A. Kabat, T. T. Wu, C. Foeller, H. M. Perry, K. S. Gottesman, *Sequences of Proteins of Immunological Interest* (DIANE Publishing, 1992).

45. T. K. Ritchie, *et al.*, “Chapter Eleven - Reconstitution of Membrane Proteins in Phospholipid Bilayer Nanodiscs” in *Methods in Enzymology*, Liposomes, Part F., N. Düzgünes, Ed. (Academic Press, 2009), pp. 211–231.

46. T. Kawate, E. Gouaux, Fluorescence-detection size-exclusion chromatography for precrystallization screening of integral membrane proteins. *Struct. Lond. Engl. 1993* **14**, 673–681 (2006).

47. K. R. Miller, *et al.*, T Cell Receptor-Like Recognition of Tumor In Vivo by Synthetic Antibody Fragment. *PLOS ONE* **7**, e43746 (2012).

48. P. K. Dominik, A. A. Kossiakoff, Phage display selections for affinity reagents to membrane proteins in nanodiscs. *Methods Enzymol.* **557**, 219–245 (2015).

49. F. A. Fellouse, *et al.*, High-throughput generation of synthetic antibodies from highly functional minimalist phage-displayed libraries. *J. Mol. Biol.* **373**, 924–940 (2007).

50. K. Zhang, Gctf: Real-time CTF determination and correction. *J. Struct. Biol.* **193**, 1–12 (2016).

51. S. H. W. Scheres, RELION: implementation of a Bayesian approach to cryo-EM structure determination. *J. Struct. Biol.* **180**, 519–530 (2012).

52. S. Q. Zheng, *et al.*, MotionCor2: anisotropic correction of beam-induced motion for improved cryo-electron microscopy. *Nat. Methods* **14**, 331 (2017).

53. A. Punjani, J. L. Rubinstein, D. J. Fleet, M. A. Brubaker, cryoSPARC: algorithms for rapid unsupervised cryo-EM structure determination. *Nat. Methods* **14**, 290–296 (2017).

54. R. Y.-R. Wang, *et al.*, Automated structure refinement of macromolecular assemblies from cryo-EM maps using Rosetta. *eLife* **5**, e17219 (2016).

55. P. Emsley, K. Cowtan, Coot: model-building tools for molecular graphics. *Acta Crystallogr. D Biol. Crystallogr.* **60**, 2126–2132 (2004).

56. P. D. Adams, *et al.*, PHENIX : a comprehensive Python-based system for macromolecular structure solution. *Acta Crystallogr. D Biol. Crystallogr.* **66**, 213–221 (2010).

57. E. F. Pettersen, *et al.*, UCSF Chimera--a visualization system for exploratory research and analysis. *J. Comput. Chem.* **25**, 1605–1612 (2004).

58. I. W. Davis, L. W. Murray, J. S. Richardson, D. C. Richardson, MOLPROBITY: structure validation and all-atom contact analysis for nucleic acids and their complexes. *Nucleic Acids Res.* **32**, W615-619 (2004).

59. B. A. Barad, *et al.*, EMRinger: side chain-directed model and map validation for 3D cryo-electron microscopy. *Nat. Methods* **12**, 943–946 (2015).

60. P. Gourdon, *et al.*, HiLiDe—Systematic Approach to Membrane Protein Crystallization in Lipid and Detergent. *Cryst. Growth Des.* **11**, 2098–2106 (2011).

61. M. D. Winn, *et al.*, Overview of the CCP4 suite and current developments. *Acta Crystallogr. D Biol. Crystallogr.* **67**, 235–242 (2011).

62. M. Strong, *et al.*, Toward the structural genomics of complexes: Crystal structure of a PE/PPE protein complex from Mycobacterium tuberculosis. *Proc. Natl. Acad. Sci.* **103**, 8060–8065 (2006).

63. W. Kabsch, Automatic processing of rotation diffraction data from crystals of initially unknown symmetry and cell constants. *J. Appl. Crystallogr.* **26**, 795–800 (1993).

64. A. J. McCoy, *et al.*, Phaser crystallographic software. *J. Appl. Crystallogr.* **40**, 658–674 (2007).

Chapter 3

Rapid screening of antibody fragments from recombinant phage display libraries using negative stain electron microscopy

Contributing Authors

Evan M. Green[1], Natalia Sevillano[2], Nancy Li[2], Charles S. Craik[2], Yifan Cheng[1,3]

[1]University of California, San Francisco, Department of Biochemistry and Biophysics

[2]University of California, San Francisco, Department of Pharmaceutical Chemistry

[3]Howard Hughes Medical Institute

Abstract

Recombinant antibodies are useful reagents in structural biology for a wide variety of proteins aiding in structure determination using single particle electron microscopy as they increase molecular weight, remove pseudosymmetry and reduce conformational flexibility. Panning for recombinant Fabs is a rapid process in which a large number of potentially useful Fabs can be identified in a short time frame. Currently screening Fabs from a panning to identify the most useful ones for structural studies is a time consuming and labor-intensive process. Here we describe a new small-scale immunoprecipitation-based method to rapidly characterize Fabs from a panning. We validate this method using three prototypical samples including a membrane protein, a multiprotein complex, and a small soluble protein. This technique provides information about the epitope that the Fab binds in addition to an estimate for the relative affinity of the Fab against an antigen. We believe this method will greatly accelerate the timeline from a panning to the structure determination of a Fab-antigen complex using single particle electron microscopy.

Introduction

Antibodies are powerful tools used to study a wide range of topics ranging from cell biology to biochemistry and structural biology due to their ability to bind a specific antigen with high affinity[1]. Traditionally antibodies have been generated using hybridoma technology where an animal is immunized with purified antigen and their B-cells are fused with myeloma cells[2]. Advances in panning for recombinant antibodies using phage display has greatly accelerated the pace at which potential binders can be found compared to animal-based immunizations[3,4]. A typical panning can produce dozens of potential binders that must be validated and characterized creating a bottleneck in the identification of useful new antigens. A number of biochemical techniques including the enzyme-linked immunosorbent assay (ELISA) can help triage initial hits but further validation is typically required to confirm complex formation between the antibody and antigen[5].

Structural biology has benefited from antibodies where they have been used as co-crystallization chaperones of difficult targets to either trap relevant conformational states or to aid in crystal contacts[6,7]. For structural studies full length antibodies are typically too flexible requiring the use of antibody fragments - such as the variable fragment (Fv) or antigen-binding fragment (Fab) - or nanobodies which are single chain Vh domains found in camelids. Recently Fabs have been used to solve the structure of numerous targets using single-particle cryogenic electron microscopy (cryoEM)[8–13]. In this role the antibodies aid as fiducial markers to increase molecular weight, break pseudosymmetry, and alter orientation distributions.

If the antibody is to be used for structural studies they need to be characterized beyond a simple ELISA to validate complex formation using other biochemical characterization such as co-elution on a size exclusion column (SEC) with the antigen. In order to generate enough

material for SEC runs it typically requires the purification of at least 100 ug of the antibody. Purification on this scale can represent a bottleneck in the screening process for many laboratories. To reduce this bottleneck in screening we have developed a new protocol taking advantage of the minimal sample requirements for negative-stain electron microscopy (nsEM) where a typical grid only requires approximately 25 ng of protein. This technique has been optimized to take advantage of the recombinant antibody panning construct design using the engineered affinity tags and expressions systems such that the phage display library does not require modification. The negative stain data collected from this new experimental protocol provides useful information about the interaction between the antibody and antigen including the location of the epitope and relative binding affinity under conditions used for subsequent structure determination.

Results and Discussion

In order to rapidly screen Fabs identified from recombinant panning using phage display libraries we developed a new immunoprecipitation-based method combined with negative stain electron microscopy. The method shown takes advantage of the observation that a small amount Fabs are secreted into the supernatant (**Figure 1**). Using the secreted Fabs we are able to do a pulldown on the myc peptide included in the original Fab panning library. To validate this approach, we applied the technique to several samples representing a wide range of proteins including a membrane protein (TmrAB), a multiprotein complex (ESCRT-I), and a small soluble protein (uPA).

As an initial validation of the new screening method we set out to characterize previously identified Fabs against the heterodimeric ABC transporter TmrAB. A previous panning against TmrAB was performed to identify Fabs against the protein to aid in the structure determination

of the psuedosymmetric protein complex using single particle cryoEM[14]. The original panning identified almost two dozen Fabs but only a small subset were extensively characterized due to the time involved in purifying the necessary quantities of protein required for traditional screening. Using the new approach, we were able to characterize 13 new Fabs against TmrAB from the initial screening (**Figure 2**). Each Fab was expressed in small scale from *E coli*. and purified using anti-myc magnetic beads. Using only 200 ng of TmrAB for each sample we could identify co-complexes using negative stain EM. The gentle elution with 0.05 mg/mL of myc peptide did not cause excessive background for negative stain. Of the 13 Fabs tested 11 yielded well resolved two-dimensional class averages indicating complex formation between the Fab and TmrAB. The remaining 2 Fabs, BC10 and CH4, had very low particle counts likely due to low affinity between TmrAB and the Fab. For 9 of the Fabs we were able to generate *ab initio* reconstructions of the TmrAB-Fab complex to gain insights into the orientation of binding relative to TmrAB. In all cases the Fab bound to the nucleotide binding domain of the transporter. Due to the resolution limits of negative stain EM it is not possible to identify whether the Fab binds to TmrA or TmrB. With the new approach we were able to characterize 14 Fabs in approximately one week including the expression, sample preparation, data collection and processing.

We next sought to test the approach for Fabs against the endosomal sorting complexes required for transport (ESCRT)-I core complex, a four protein heterotetrameric assembly[15]. Similar to the approach described for TmrAB we were able to validate the method against previously characterized Fabs (**Figure 3**). From the 2D class averages it is clear that CB4 and DD11 bind the hinge between the stalk and the headpiece while DB8 binds only the headpiece.

With these complexes *ab initio* structure determination was not successful, likely due to the high flexibility of the ESCRT-I complex.

Finally, we wanted to characterize the ability of the approach with a small soluble protein. We decided to use uPA, which is approximately 25 kDa, for this test as a series of Fabs with inhibitory properties had been generated from the parental Fab U33 with a wide range of affinities[16]. Initial characterization of the uPA-Fab complexes revealed a tri-lobed structure characteristic of the expected architecture (**Figure 4**). When analyzing the data, we observed that the number of particles in the full uPA-Fab complex seemed to correlate with the relative affinity of the Fabs making us wonder if it would be possible to directly estimate the relative affinities of the Fabs from the negative stain data. In order to estimate the affinities of the various Fabs we took advantage of the single particle nature of the data. First, we generated reference volumes for the Fab, uPa, and uPA-Fab complex using cryoSPARC from manually selected 2D class averages. Then, we merged all of the data sets together and performed a round of heterogenous refinement to classify each particle into one of the three classes. Using the particle counts for each sample it was possible to estimate the affinity by noting that the dissociation constant (Kd) is given by the following equation:

$$Kd = [uPA][Fab] / [uPA\text{-}Fab] \quad \text{(eq. 1)}$$

If we assume that the particle counts for the negative stain data are proportional to the concentrations of species in solution we can estimate the relative Kd from a single concentration as we directly observe all required parameters. Using these results, we could then compare the estimated Kd values from the EM data with previously determined Kd values. From this we observed a high degree of correlation between the estimated and experimentally determined

values suggesting it is possible to directly estimate the relative affinities of each Fab from single particle counting.

Conclusions

Taking advantage of negative stain EM we were able to create a new simple protocol for the rapid characterization of Fabs identified from phage display panning. Using this method we show that it provides comparable results to previous methods where each Fab is purified in large quantity before forming a complex with the antigen. This approach makes it possible to not only characterize if an identified Fab is a true binder but also gives information into the epitope that the Fab binds. Additionally, we show that directly from the negative stain data it is possible to estimate the relative affinity of the Fabs from a sample at a single concentration. This new method greatly improves the speed at which Fabs can be characterized and used for further structural studies decreasing the time-consuming bottleneck of validating Fabs after a panning.

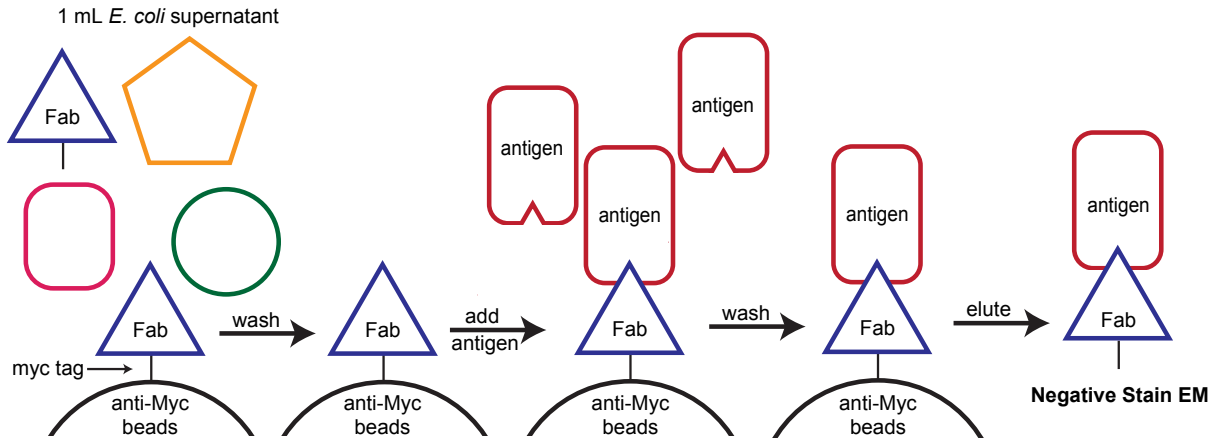

Figure 3.1: Overview of small-scale immunoprecipitation-based screening of Fabs from recombinant phage display libraries. Individual clones are picked and Fabs are expressed in small scale. Fabs secreted into the supernatant are bound to anti-myc magnetic beads and thoroughly washed. Antigen is added to form a complex with the Fab and unbound antigen is removed. The Fab-antigen complex is eluted with myc peptide and used directly to make negative stain EM grids for subsequent screening.

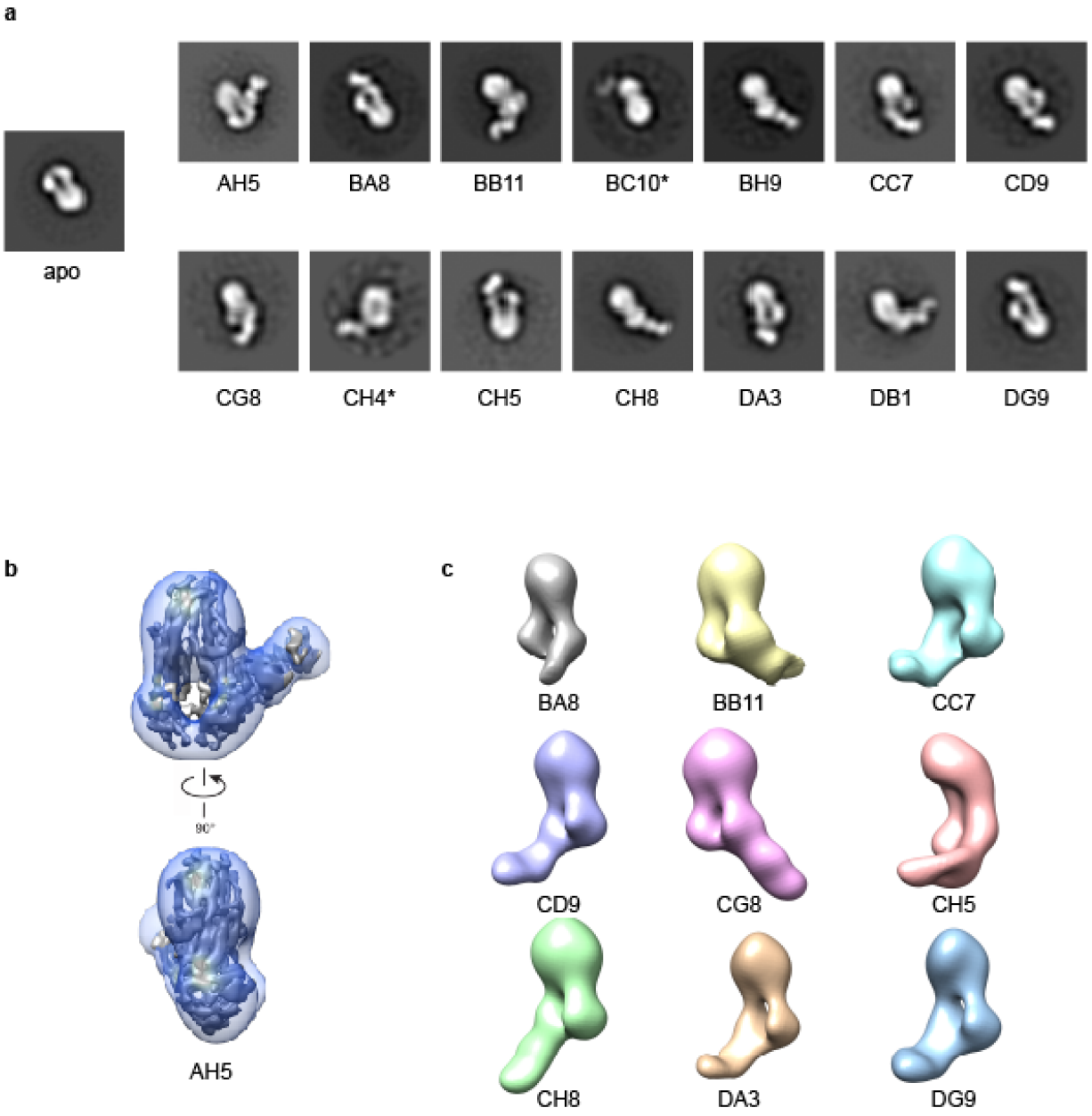

Figure 3.2: Screening Fabs against the heterodimeric ABC transporter TmrAB. Fabs from a panning against TmrAB were screened using the immunoprecipitation approach. (**a**) Two-dimensional class averages of apo TmrAB and complexes between a number of unique Fabs. Antibodies marked with an asterisk (*) had extremely low particle counts and likely represent false positives or antibodies with low affinity. (**b**) Three-dimensional reconstruction of TmrAB bound to the previously reported antibody AH5. The volume in transparent blue is from negative stain EM data collected in this report with the cryoEM structure of TmrAB from EMDB-6085 shown in grey. (**c**) Three dimensional reconstructions of TmrAB-Fab complexes from negative stain EM.

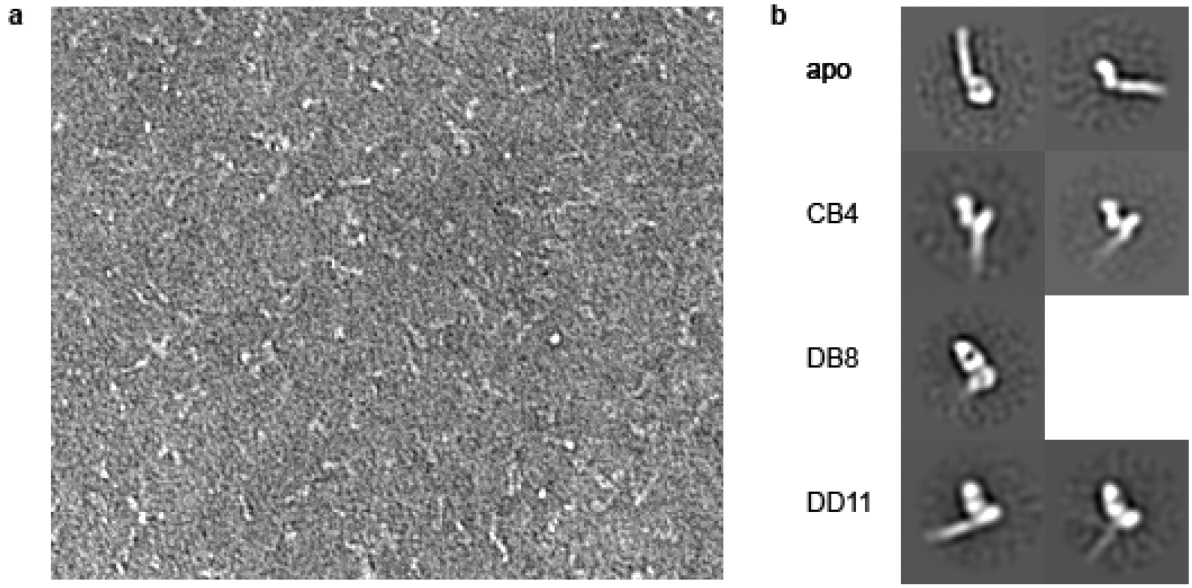

Figure 3.3: Fabs against the ESCRT-I core complex. (**a**) Micrograph of ESCRT-I core complex with DD11. (**b**) Two-dimensional class averages of Fabs against the ESCRT-I core complex.

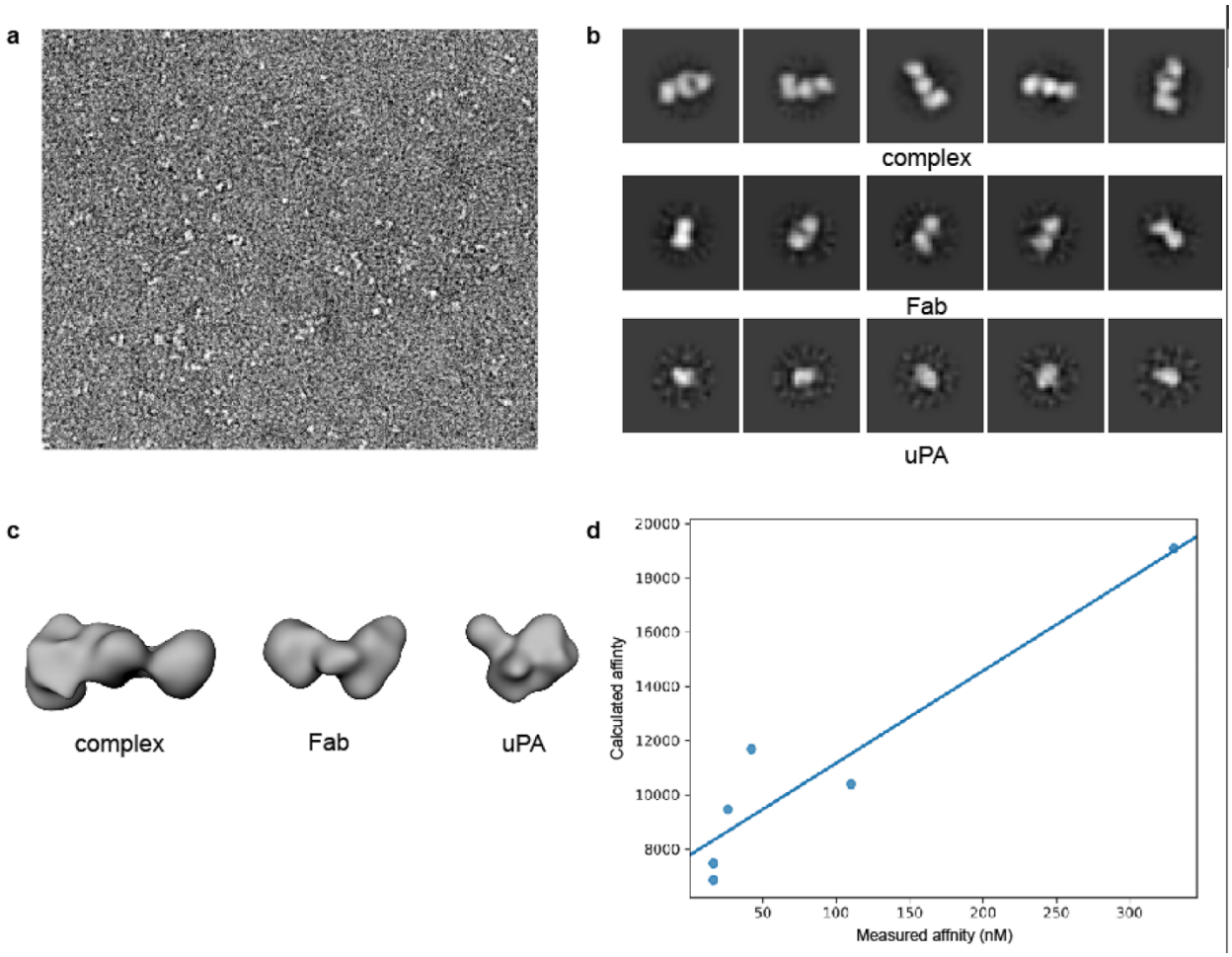

Figure 3.4: Analysis for affinity matured Fabs against uPA. (**a**) Representative micrographs of negatively stained sample from the uPA-Fab pulldown. (**b**) Representative two-dimensional class averages of uPA-Fab complexes, Fab alone, and uPA alone. (**c**) Three dimensional volumes for uPA-Fab complex, Fab, and uPA used for heterogeneous classification in cryoSPARC. (**d**) Comparison of experimentally measured affinity of Fabs and calculated affinity from heterogenous refinement.

Methods

Immunoprecipitation of antibody fragments. For the small-scale immunoprecipitation of Fabs 1 mL of *E. coli* supernatant expression individual Fabs was mixed with 5 uL of anti-c-myc magnetic beads pre-washed in HBS (20 mM Hepes pH 7.5, 150 mM NaCl). The supernatant and beads were incubated for 2 hours at 4C with rotations. After binding the beads were washed three times with 1 mL of HBS. Following the wash 10 uL of antigen was added at a concentration of 0.2 mg/mL and incubated with the beads for 30 minutes at 4C. Unbound antigen was removed by washing two times with 1 mL of HBS. Samples were eluted with 10 uL of HBS supplemented with 0.1 mg/mL c-myc peptide.

Negative stain electron microscopy. The immunoprecipitation eluent was used directly to make uranyl formate stained grids according to previously published protocols. Samples were imaged on a Tecnai T20 microscope equipped with a TVIPS 8kx8k camera at a magnification of either 50kx or 80kx yielding a nominal magnification of 1.2 or 1.57 Å, respectively. TmrAB samples were imaged at 50kx magnification and uPA and ESCRT-I samples were imaged at 80kx magnification. All data were binned 2x directly from the camera.

Negative stain data processing. CTF parameters were estimated using gctf and particles were picked using gautomatch. Two-dimensional class averages were generated using Relion. For the uPA samples reference volumes for heterogenous refinement were determined using the *ab initio* feature of cryoSPARC with manually selected 2D classes. After a round of 2D classification to remove bad particles a round of heterogenous refinement was done to classify each particle as either uPA alone, Fab alone, or the uPA-Fab complex.

References

1. Basu, K., Green, E. M., Cheng, Y. & Craik, C. S. Why recombinant antibodies - benefits and applications. *Curr. Opin. Biotechnol.* **60**, 153–158 (2019).
2. Kohler, G. & Milstein, C. Continuous cultures of fused cells secreting antibody of predefined specificity. *Nature* **256**, 495–497 (1975).
3. Hoogenboom, H. R. *et al.* Antibody phage display technology and its applications. *Immunotechnology* **4**, 1–20 (1998).
4. Chao, G. *et al.* Isolating and engineering human antibodies using yeast surface display. *Nat. Protoc.* **1**, 755–768 (2006).
5. Suter, L., Bruggen, J. & Sorg, C. Use of an enzyme-linked immunosorbent assay (ELISA) for screening of hybridoma antibodies against cell surface antigens. **39**, 407–411 (1980).
6. Li, X. *et al.* Structure-Function Analysis of the Extended Conformation of a Polyketide Synthase Module. *J. Am. Chem. Soc.* **140**, 6518–6521 (2018).
7. Zhou, Y., Morais-Cabral, J. H., Kaufman, A. & MacKinnon, R. Chemistry of ion coordination and hydration revealed by a K+ channel-Fab complex at 2.0 A resolution. *Nature* **414**, 43–48 (2001).
8. Liang, Y. L. *et al.* Phase-plate cryo-EM structure of a class B GPCR-G-protein complex. *Nature* **546**, 118–123 (2017).
9. Zhang, Y. *et al.* Cryo-EM structure of the activated GLP-1 receptor in complex with a G protein. *Nature* **546**, 248–253 (2017).
10. Kang, Y. *et al.* Cryo-EM structure of human rhodopsin bound to an inhibitory G protein. *Nature* **558**, 553–558 (2018).
11. Cormier, A. *et al.* Cryo-EM structure of the αvβ8 integrin reveals a mechanism for

stabilizing integrin extension. *Nat. Struct. Mol. Biol.* **25**, (2018).

12. Taylor, N. M. I. *et al.* Structure of the human multidrug transporter ABCG2. *Nature* **546**, 504–509 (2017).

13. Dang, S. *et al.* Cryo-EM structures of the TMEM16A calcium-activated chloride channel. *Nature* **552**, 426–429 (2017).

14. Kim, J. *et al.* Subnanometre-resolution electron cryomicroscopy structure of a heterodimeric ABC exporter. *Nature* **517**, 396–400 (2015).

15. Kostelansky, M. S. *et al.* Structural and Functional Organization of the ESCRT-I Trafficking Complex. *Cell* **125**, 113–126 (2006).

16. LeBeau, A. M. *et al.* Imaging active urokinase plasminogen activator in prostate cancer. *Cancer Res.* **75**, 1225–1235 (2015).

Publishing Agreement

It is the policy of the University to encourage the distribution of all theses, dissertations, and manuscripts. Copies of all UCSF theses, dissertations, and manuscripts will be routed to the library via the Graduate Division. The library will make all theses, dissertations, and manuscripts accessible to the public and will preserve these to the best of their abilities, in perpetuity.

Please sign the following statement:

I hereby grant permission to the Graduate Division of the University of California, San Francisco to release copies of my thesis, dissertation, or manuscript to the Campus Library to provide access and preservation, in whole or in part, in perpetuity.

DocuSigned by:
Green, Evan M
D7529F7CFD8A48C...

Author Signature

12/17/2019

Date